electronics

MDPI

Article

Low-Carbon Optimal Scheduling of High-Altitude Construction-Park Integrated Energy System Considering Truck–Grid Interaction

Zhijian Liu [1,2], Cheng Cheng [1], Xudong Yang [1,2,*] and Shijie Huang [1]

[1] Faculty of Electric Power Engineering, Kunming University of Science and Technology, Kunming 650093, China; zhangshuailong@stu.kust.edu.cn (C.C.)
[2] Faculty of Transportation Engineering, Kunming University of Science and Technology, Kunming 650093, China
* Correspondence: 20241106005@stu.kust.edu.cn

Abstract

As green power systems continue to develop, an increasing number of power generation and energy storage facilities are being constructed in high-altitude regions. However, existing microgrid-based energy supply architectures in high-altitude construction parks face low energy utilization efficiency, high carbon emissions, and inadequate accounting for market-related costs. To address these issues, this study proposes a low-carbon optimal dispatch method incorporating truck–grid interaction for a high-altitude construction-park integrated energy system (HACP-IES). First, a coupled waste heat recovery–organic Rankine cycle–power-to-gas (WHR–ORC–P2G) model and a multi-state transition model for construction electric heavy-duty trucks (CEHTs) are developed to enable the cascade utilization of waste heat and coordinated operation of mobile energy storage. Second, a dynamic green certificate–carbon trading interaction mechanism and multi-energy demand response are introduced to exploit flexibility through market incentives and demand-side adjustments, while wind and photovoltaic forecast uncertainties are addressed using chance constraints under a normal distribution assumption. Finally, a multi-objective mixed-integer linear programming model is formulated and solved, with normalized linear weighting used to balance operating cost and actual carbon emissions. Comparative analyses across multiple scenarios show that, with all coordinated resources participating, the proposed method reduces operating cost and carbon emissions by 78.02% and 32.22%, respectively, relative to the benchmark, thereby improving both the economic and low-carbon performance of the park's energy system.

Keywords: truck–grid interaction; low-carbon optimal scheduling; dynamic green certificate and carbon trading mechanism; high-altitude construction-park integrated energy system; multi-state transition model; construction electric heavy-duty trucks

Check for updates

Academic Editor: Herminio Martínez-García

Received: 29 September 2026
Revised: 23 October 2026
Accepted: 27 October 2026
Published: 29 October 2026

Copyright: © 2026 by the authors. Licensee MDPI, Basel, Switzerland. This article is an open access article distributed under the terms and conditions of the Creative Commons Attribution (CC BY) license.

1. Introduction

Driven by China's "dual-carbon" goals, the number of large-scale integrated wind–solar–storage renewable energy station projects is increasing [1,2]. Considering specific land costs and the output characteristics of wind and solar power, these large-scale renewable generation and storage projects are predominantly located in sparsely populated high-altitude regions. During the construction phase, temporary construction parks featuring a "microgrid" structure are often established on site to optimize energy efficiency over long

construction periods [3]. However, the energy systems of these simple microgrid-structured parks [4,5] face limitations in operational flexibility and fail to consider the coordinated utilization of internal flexibility resources. Therefore, it is imperative to further find an effective energy system framework and dispatch method for HACPs.

As a novel energy utilization architecture, the IES offers notable advantages in terms of multi-energy complementarity and efficient energy utilization. Therefore, constructing an HACP-IES can effectively improve the economic performance of energy utilization in construction operations. In recent years, extensive studies have been conducted on the economic dispatch of IESs. Existing research mainly focuses on optimizing energy equipment configurations, enhancing dispatch security, and exploiting the flexibility of internal resources. For instance, Ref. [6] proposed an integrated energy supply unit comprising internal combustion engines, gas boilers, heat exchangers, electricity supply, and cooling equipment. By coordinating energy exchanges among multiple devices, the unit can improve the operational economy of the system. Ref. [7] developed a unified modeling framework for energy storage devices and user-side adjustable resources in an IES and established a generalized energy storage optimization model, thereby improving the utilization of flexible resources while reducing the dimensionality of the decision variables. Ref. [8] further investigated refined operating constraints and multi-time-scale dispatch strategies for different energy storage technologies to enhance the utilization efficiency of hybrid energy storage systems. However, the aforementioned studies mainly focus on improving equipment utilization and do not sufficiently quantify the dispatch risks caused by source load fluctuations [9–14]. Owing to the complex operating environment of the HACP-IES, conventional deterministic dispatch methods may fail to adequately guarantee secure system operation. Therefore, robust optimization methods are required to address internal source load uncertainties and improve the security of dispatch decisions. Regarding the modeling of wind and solar uncertainties, Ref. [12] considered the differences in uncertainty characteristics between the day-ahead and intra-day dispatch stages. Specifically, box uncertainty sets were employed in the day-ahead stage to characterize source-side uncertainties and enhance strategy robustness, while stochastic optimization was adopted in the intra-day stage to correct the real-time impacts of renewable output deviations. Ref. [14] incorporated the decision maker's risk tolerance into the optimization model based on information gap decision theory (IGDT), thereby achieving, to some extent, a balance between robustness and economy. Nevertheless, these approaches generally impose robustness at the system level and pay insufficient attention to the capability of internal flexible resources, particularly mobile energy storage resources, to mitigate wind and solar power fluctuations. As a result, the dispatch flexibility of the system cannot be fully exploited.

In practice, an IES contains various flexible resources, including electric vehicles (EVs), electric heavy-duty trucks, and virtual power plants (VPPs) [15–30]. These resources can be used during system operation by providing appropriate dispatch compensation, thereby helping balance the trade-off between security and economy. Specifically, Ref. [24] proposed an optimal grid dispatch strategy that coordinates the charging schedules of EVs and electric heavy-duty trucks according to meteorological conditions, local electricity prices, and grid accommodation capability, demonstrating that the participation of such flexible resources can effectively reduce the overall system operating cost. Ref. [27] investigated the dispatchability of industrial electric heavy-duty trucks and proposed a coordinated truck–grid dispatch strategy, showing that their participation can effectively enhance renewable energy accommodation. However, the above studies do not fully consider the operating-state constraints of these flexible resources during dispatch. In the HACP-IES, construction electric heavy-duty trucks must simultaneously participate in energy interaction and fulfill

their mandatory transportation tasks. Therefore, a dedicated operating-state model is required to accurately characterize their dispatchable behavior.

In summary, research specifically addressing the HACP-IES remains limited. Compared with conventional IESs, the HACP-IES exhibits distinct oxygen demand characteristics. Moreover, owing to the high-altitude and cold construction environment, thermal loads account for a relatively large proportion of the total energy demand, while the overall load fluctuation characteristics are more complex. Consequently, dispatch methods developed for conventional IESs may have limited applicability to the HACP-IES. To address these issues, this paper proposes an optimal dispatch method for the HACP-IES considering truck–grid interaction. The main contributions are summarized as follows:

1. Multi-energy coupling and flexible resource modeling: Mathematical models of CEHTs, WCHPU, and WHR–ORC–P2G are developed to characterize the energy coupling relationships of the HACP-IES and facilitate the coordinated utilization of mobile storage, construction waste, and recovered heat.
2. Market and demand-side coordination: A dynamic GC–CT interaction mechanism and multi-energy demand response are introduced to coordinate market incentives, demand-side flexibility, and carbon emission regulation.
3. Low-carbon economic dispatch: An optimal scheduling model is established to minimize the operating cost of the HACP-IES. Multi-scenario case studies evaluate its effectiveness in reducing operating costs and carbon emissions while promoting renewable energy utilization.

2. HACP-IES Scheduling Framework and Key Equipment Models

2.1. HACP-IES Scheduling Framework

To enhance the energy utilization efficiency of the HACP, this work proposes an HACP-IES framework that integrates electrical, thermal, gas, and oxygen loads, together with a P2G facility and vacuum pressure swing adsorption unit (VPSAU). The proposed framework considers the utilization of by-product oxygen and waste heat recovery from the P2G process while exploiting the mobile energy storage capability of CEHTs and the energy recovery potential of construction waste to enhance the flexibility of energy resource allocation and system operation during HACP-IES operation. The detailed framework is presented in Figure 1.

As illustrated in Figure 1, the HACP electrical load is primarily met by the power grid, wind turbine (WT), photovoltaic (PV) unit and WCHPU. The heat load is supplied by the gas boiler (GB), electric boiler (EB), WCHPU and waste heat boiler (WHB). The gas load is supplied jointly by the gas network (GN) and the methanation reactor (MR) within the P2G unit. The oxygen load is primarily met by the VPSAU and the by-product oxygen generated during the P2G process. At the same time, the system is equipped with various types of energy storage devices—including those for electricity, heat, gas, oxygen and hydrogen—to enhance the HACP-IES's ability to regulate energy fluctuations. Furthermore, this work proposes a dynamic green certificate and carbon trading mechanism (DGCACTM) and introduces the multi-energy demand response mechanism (MDRM) to enhance system energy utilization efficiency from the market-based regulation and use demand-side perspectives, respectively, thereby achieving the coordinated optimization of the HACP-IES in terms of economic performance, operational flexibility, and low-carbon performance.

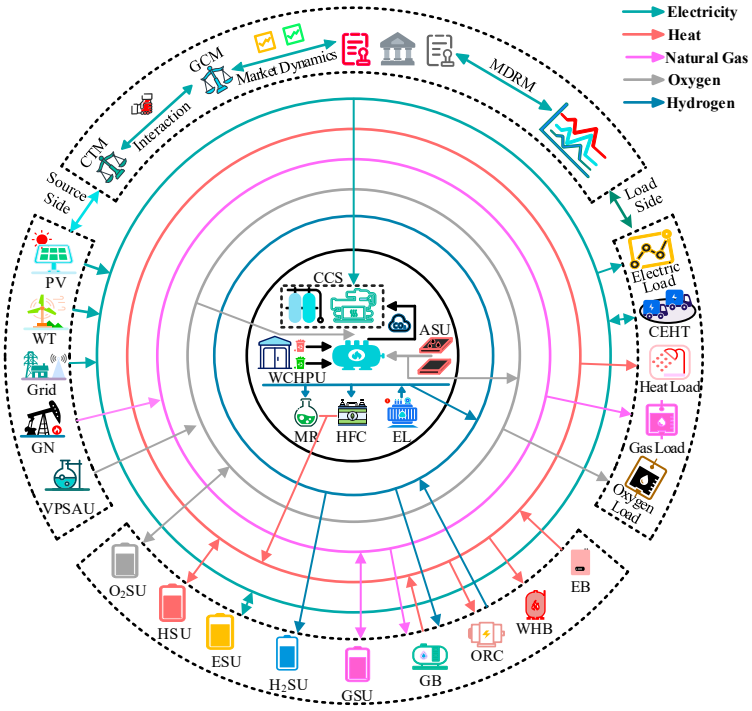

Figure 1. HACP-IES scheduling framework.

2.2. Key Equipment Models

The key components of the proposed framework include CEHTs, a P2G unit with waste heat recovery, and a WCHPU. The CEHTs exploit their mobile energy storage capability to participate in coordinated IES scheduling, thereby facilitating wind and photovoltaic power accommodation through their flexible charging and discharging actions. For the P2G process, the generated waste heat is further recovered for direct heat supply and electricity generation through an organic Rankine cycle (ORC), enabling the cascade utilization of waste heat and improving the overall energy efficiency and operational economy of the P2G unit. In addition, to utilize the construction waste generated during HACP construction, a WCHPU is incorporated to recover its energy content for combined electricity and heat production, thereby improving the overall energy-use efficiency and economic performance of the HACP.

2.2.1. Model of CEHTs

Based on multi-state system modeling theory [22], a mathematical model for the CEHTs in the HACP is established. Each CEHT is modeled with six operating states: charging (1), discharging (2), transportation (3), loading (4), unloading (5), and standby (6). The logical relationships governing the transitions among the operating states are illustrated in Figure 2. Based on the CEHT states, the relevant constraints for the CEHTs in the HACP can be established.

Firstly, it is necessary to ensure that at any given moment, a CEHT is in only one operational state.

$$\begin{cases} \sum_{s=1}^{N_s} x_{i,s,t}^{\mathrm{CEHT}} \\ x_{i,t}^{\mathrm{CEHT}} \in \{0,1\} \\ i \in \Omega_{\mathrm{CEHT}}, \end{cases} \tag{1}$$

where $x_{i,s,t}^{\mathrm{CEHT}}$ is the binary variable for the operating states of the CEHT; N_s is the number of operating states of each CEHT; Ω_{CEHT} is the set of the CEHTs within the HACP.

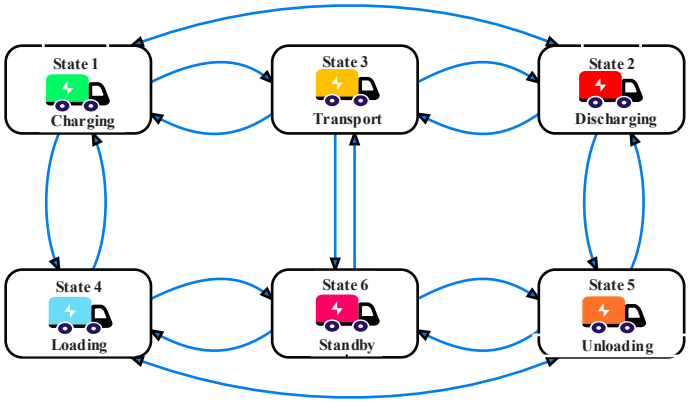

Figure 2. Operating-state transition diagram of CEHTs.

Secondly, let S denote the set of permitted transition states for CEHTs across time periods. The process of state transition for CEHTs must satisfy the following constraints.

$$\begin{cases} x_{i,s,t+1}^{\mathrm{CEHT}} + x_{i,\hat{s},t}^{\mathrm{CEHT}} \le 1, \ \forall (s,\hat{s}) \notin S \\ S = \{(1,1),(1,2),(1,3),(1,6),(2,1),(2,2),(2,3),(2,6),(3,3), \\ (3,4),(3,5),(3,6),(4,3),(4,4),(5,3),(5,5),(5,6),(6,1),(6,2), \\ (6,3),(6,6)\}, \end{cases} \tag{2}$$

where $x_{i,s,t}^{\mathrm{CEHT}}$ and $x_{i,\hat{s},t}^{\mathrm{CEHT}}$ are binary variables indicating whether CEHT i operates in a state.

The matrix form of the state transition constraint for (2) is

$$\begin{cases} \boldsymbol{x}_{i,t}^{\mathrm{CEHT}} = \left[x_{i,1,t}^{\mathrm{CEHT}}, x_{i,2,t}^{\mathrm{CEHT}}, \ldots, x_{i,6,t}^{\mathrm{CEHT}}\right]^{\mathrm{T}} \\ \boldsymbol{x}_{i,t+1}^{\mathrm{CEHT}} \le \boldsymbol{A}\boldsymbol{x}_{i,t}^{\mathrm{CEHT}} \\ \boldsymbol{A} = \begin{bmatrix} 1 & 1 & 1 & 0 & 0 & 1 \\ 1 & 1 & 1 & 0 & 0 & 1 \\ 1 & 1 & 1 & 1 & 1 & 1 \\ 0 & 0 & 1 & 1 & 0 & 0 \\ 1 & 1 & 1 & 0 & 1 & 1 \\ 1 & 1 & 1 & 1 & 0 & 1 \end{bmatrix} \end{cases} \tag{3}$$

where $\boldsymbol{x}_{i,t}^{\mathrm{CEHT}}$ is the state vector of the CEHT, and $\boldsymbol{A}$ is the state transition matrix of the CEHT.

Next, consideration must be given to the relationship between the battery capacity of CEHTs and their operating conditions, namely the following:

$$\begin{cases} 0 \le P_{i,t,\mathrm{char}}^{\mathrm{CEHT}} \le x_{i,1,t}^{\mathrm{CEHT}} P_{i,\mathrm{max,char}}^{\mathrm{CEHT}} \\ 0 \le P_{i,t,\mathrm{disc}}^{\mathrm{CEHT}} \le x_{i,2,t}^{\mathrm{CEHT}} P_{i,\mathrm{max,disc}}^{\mathrm{CEHT}} \\ E_{i,t+1}^{\mathrm{CEHT}} = E_{i,t}^{\mathrm{CEHT}} + \eta_i^{\mathrm{char}} P_{i,t,\mathrm{char}}^{\mathrm{CEHT}} \Delta t - \frac{P_{i,t,\mathrm{disc}}^{\mathrm{CEHT}}}{\eta_i^{\mathrm{disc}}} \Delta t - E_i^{\mathrm{tra}} x_{i,3,t}^{\mathrm{CEHT}} - E_i^{\mathrm{loa}} x_{i,4,t}^{\mathrm{CEHT}} - E_i^{\mathrm{unl}} x_{i,5,t}^{\mathrm{CEHT}} \\ E_{i,\min}^{\mathrm{CEHT}} \le E_{i,t}^{\mathrm{CEHT}} \le E_{i,\max}^{\mathrm{CEHT}}, \end{cases} \tag{4}$$

where $P_{i,\mathrm{max,char}}^{\mathrm{CEHT}}$ and $P_{i,\mathrm{max,disc}}^{\mathrm{CEHT}}$ denote the maximum charging and discharging powers of CEHT i, respectively; $P_{i,t,\mathrm{char}}^{\mathrm{CEHT}}$ and $P_{i,t,disc}^{\mathrm{CEHT}}$ are the charging and discharging powers of CEHT i, respectively; η_i^{char} and η_i^{disc} denote the charging and discharging efficiencies, respectively; E_i^{tra}, E_i^{loa}, and E_i^{unl} denote the SOC consumption during transportation, loading, and unloading, respectively; and $E_{i,\max}^{\mathrm{CEHT}}$ and $E_{i,\min}^{\mathrm{CEHT}}$ denote the maximum and minimum SOC limits of CEHT i, respectively.

$$\begin{cases} E_{i,t}^{\mathrm{tra}} = (m_i + q_{i,t}) L_{i,t} \mu_i \\ E_{i,t}^{\mathrm{loa}} = P_i^{\mathrm{aux,loa}} \tau_i^{\mathrm{loa}} \\ E_{i,t}^{\mathrm{unl}} = P_i^{\mathrm{aux,unl}} \tau_i^{\mathrm{unl}} \end{cases} \tag{5}$$

where $m_i, q_{i,t}, L_{i,t}$ denote the unladen mass, actual transportation payload, and transportation average distance, respectively; μ_i denotes the energy consumption conversion coefficient considering drive efficiency; τ_i^{loa} denotes the time used for loading; $P_i^{\mathrm{aux,loa}}$ denotes the loading power consumption of CEHT i; τ_i^{unl} denotes the time used for unloading; and $P_i^{\mathrm{aux,unl}}$ denotes the power consumption of CEHT i during unloading.

Finally, CEHTs must meet requirements regarding vehicle downtime and the need to transport materials on site.

$$\begin{cases} \sum\limits_{t\in T} x_{i,6,t}^{\mathrm{CEHT}} \geq t_{\mathrm{res}} \\ 0 \leq m_{i,\mathrm{loa}}^{\mathrm{CEHT}} \leq M_{i,\mathrm{loa}}^{\mathrm{CEHT}} x_{i,4,t}^{\mathrm{CEHT}} \\ 0 \leq m_{i,\mathrm{unl}}^{\mathrm{CEHT}} \leq M_{i,\mathrm{unl}}^{\mathrm{CEHT}} x_{i,5,t}^{\mathrm{CEHT}} \\ L_{i,t}^{\mathrm{CEHT}} = L_{i,t-1}^{\mathrm{CEHT}} + m_{i,\mathrm{loa}}^{\mathrm{CEHT}} - m_{i,\mathrm{unl}}^{\mathrm{CEHT}} \\ 0 \leq L_{i,t}^{\mathrm{CEHT}} \leq L_{i,\mathrm{max}}^{\mathrm{CEHT}} \\ L_{i,t}^{\mathrm{CEHT}} \leq L_{i,\mathrm{max}}^{\mathrm{CEHT}} \left(x_{i,3,t}^{\mathrm{CEHT}} + x_{i,4,t}^{\mathrm{CEHT}} + x_{i,5,t}^{\mathrm{CEHT}} \right) \\ \sum\limits_{i\in\Omega_{\mathrm{CEHT}}} m_{i,\mathrm{unl}}^{\mathrm{CEHT}} \geq D_t^{\mathrm{tra}} \end{cases} \tag{6}$$

where t_{res} denotes the required daily rest period of CEHT i; $M_{i,\mathrm{loa}}^{\mathrm{CEHT}}$ and $M_{i,\mathrm{unl}}^{\mathrm{CEHT}}$ represent the maximum loading and unloading quantities of CEHT i, respectively; $L_{i,t}^{\mathrm{CEHT}}$ and $L_{i,\mathrm{max}}^{\mathrm{CEHT}}$ denote the transported material quantity and maximum payload capacity of CEHT i, respectively; and D_t^{tra} denotes the construction material demand of the HACP.

2.2.2. Model of WCHPU

The WCHPU converts construction waste into thermal and electrical energy to meet part of the park's energy demand while operating subject to waste storage, power output, and ramping constraints.

$$\begin{cases} \begin{cases} P_t^{\mathrm{e,WCHPU}} = P_{t,\mathrm{tot}}^{\mathrm{e,WCHPU}} - P_{t,\mathrm{loss}}^{\mathrm{e,WCHPU}} \\ P_{t,\mathrm{loss}}^{\mathrm{e,WCHPU}} = P_{\mathrm{CCS},t}^{\mathrm{e,WCHPU}} + P_{\mathrm{bas}}^{\mathrm{e,WCHPU}} \\ P_{\mathrm{min}}^{\mathrm{e,WCHPU}} \leq P_t^{\mathrm{e,WCHPU}} \leq P_{\mathrm{max}}^{\mathrm{e,WCHPU}} \\ k_{\mathrm{min}}^{\mathrm{WCHPU}} P_t^{\mathrm{e,WCHPU}} \leq P_t^{\mathrm{h,WCHPU}} \leq k_{\mathrm{max}}^{\mathrm{WCHPU}} P_t^{\mathrm{e,WCHPU}} \end{cases} \\ \left| P_t^{\mathrm{e,WCHPU}} - P_{t-1}^{\mathrm{e,WCHPU}} \right| \leq R_{\mathrm{max}}^{\mathrm{WCHPU}} \\ \begin{cases} M_t^{\mathrm{WCHPU}} = \eta_{\mathrm{e}}^{\mathrm{WCHPU}} P_{t,\mathrm{tot}}^{\mathrm{e,WCHPU}} + \eta_{\mathrm{h}}^{\mathrm{WCHPU}} P_t^{\mathrm{h,WCHPU}} \\ M_{\mathrm{min}}^{\mathrm{WCHPU}} \leq M_t^{\mathrm{WCHPU}} \leq M_{\mathrm{max}}^{\mathrm{WCHPU}} \\ S_1^{\mathrm{WCHPU}} = S_{\mathrm{init}}^{\mathrm{WCHPU}} \\ S_t^{\mathrm{WCHPU}} - S_{t-1}^{\mathrm{WCHPU}} = M_t^{\mathrm{WCHPU}} \\ S_{\mathrm{min}}^{\mathrm{WCHPU}} \leq S_t^{\mathrm{WCHPU}} \leq S_{\mathrm{max}}^{\mathrm{WCHPU}} \end{cases} \end{cases} \tag{7}$$

where $P_{t,\mathrm{tot}}^{\mathrm{e,WCHPU}}$, $P_t^{\mathrm{e,WCHPU}}$, and $P_{t,\mathrm{loss}}^{\mathrm{e,WCHPU}}$ denote the total electrical power, electrical power, and electrical power loss of the WCHPU, respectively; $P_{\mathrm{CCS},t}^{\mathrm{e,WCHPU}}$ and $P_{\mathrm{bas}}^{\mathrm{e,WCHPU}}$ denote the power consumed by the CCS installed on the WCHPU and its base power loss, respectively; $P_t^{\mathrm{h,WCHPU}}$ denotes the thermal power of the WCHPU; $k_{\mathrm{min}}^{\mathrm{WCHPU}}$ and $k_{\mathrm{max}}^{\mathrm{WCHPU}}$ denote the minimum and maximum heat-to-power ratios, respectively; $R_{\mathrm{max}}^{\mathrm{WCHPU}}$ denotes the maximum ramping power; $\eta_{\mathrm{e}}^{\mathrm{WCHPU}}$ and $\eta_{\mathrm{h}}^{\mathrm{WCHPU}}$ denote the amounts of waste consumed per unit of electrical and thermal power output, respectively; M_t^{WCHPU} denotes the amount of waste consumed by the WCHPU; $M_{\mathrm{min}}^{\mathrm{WCHPU}}$ and $M_{\mathrm{max}}^{\mathrm{WCHPU}}$ denote the minimum and maximum amounts of waste, respectively; S_t^{WCHPU} denotes the amount of waste stored in the WCHPU; $S_{\mathrm{min}}^{\mathrm{WCHPU}}$ and $S_{\mathrm{max}}^{\mathrm{WCHPU}}$ denote the minimum and maximum waste storage capacities of the WCHPU, respectively.

To reduce the carbon emissions from the WCHPU, a flexible CCS system is integrated with the unit to capture and store emitted CO_2. The operating constraints of the CCS system are expressed as follows:

$$\begin{cases} P_t^{\mathrm{e,CCS}} = \alpha_{\mathrm{D}}\beta_{\mathrm{C}}\lambda_{\mathrm{E}}\delta_{\mathrm{E}}P_{t,\mathrm{tot}}^{\mathrm{e,WCHPU}} + P_{t,\mathrm{ana}}^{\mathrm{e,CCS}} \\ P_{\min}^{\mathrm{e,CCS}} \le P_t^{\mathrm{e,CCS}} \le P_{\max}^{\mathrm{e,CCS}} \\ m_{t,\mathrm{com}}^{\mathrm{CO_2}} = \alpha_{\mathrm{D}}\beta_{\mathrm{C}}P_{t,\mathrm{tot}}^{\mathrm{e,WCHPU}} - \lambda_{\mathrm{ana}}P_{t,\mathrm{ana}}^{\mathrm{e,CCS}} \\ V_t^{\mathrm{CSS}} = \frac{m_{\mathrm{t,com}}^{\mathrm{CO_2}} m_{\mathrm{MEA}}}{\rho_{\mathrm{MEA}}\omega_{\mathrm{MEA}}\theta_{\mathrm{CSS}}m_{\mathrm{CO_2}}} \\ V_{\mathrm{R},t}^{\mathrm{CSS}} = V_{\mathrm{R},t-1}^{\mathrm{CSS}} - V_t^{\mathrm{CSS}} \\ V_{\mathrm{M},t}^{\mathrm{CSS}} = V_{\mathrm{M},t-1}^{\mathrm{CSS}} + V_t^{\mathrm{CSS}} \\ 0 \le V_{\mathrm{R},t}^{\mathrm{CSS}} \le V_{\max}^{\mathrm{CCS}} \\ 0 \le V_{\mathrm{M},t}^{\mathrm{CSS}} \le V_{\max}^{\mathrm{CCS}} \end{cases} \tag{8}$$

where α_{D}, β_{C}, λ_{C} and δ_{E} denote the flue-gas split ratio, carbon-capture intensity, energy consumption coefficient of the CCS system, and carbon emission factor of the WCHPU, respectively; m_{MEA} and $m_{\mathrm{CO_2}}$ denote the molar masses of monoethanolamide (MEA) and CO_2, respectively; ρ_{MEA}, ω_{MEA} and θ_{CSS} denote the density and concentration of the MEA solution and the desorption capacity of the CCS stripper, respectively; $V_{\mathrm{R},t}^{\mathrm{CSS}}$ and $V_{\mathrm{M},t}^{\mathrm{CSS}}$ denote the liquid volumes in the rich- and lean-solvent tanks of the CCS system, respectively; and $V_{i,\max}^{\mathrm{CCS}}$ denotes the maximum volume of the captured CO_2 solution.

2.2.3. WHR-ORC-P2G Model

Building upon the conventional P2G model, this work further considers waste heat recovery from the P2G process and the utilization of by-product oxygen generated during hydrogen production in the electrolyzer (EL). By incorporating an ORC for waste-heat-to-power conversion, an enhanced WHR-ORC-P2G is developed.

The hydrogen and oxygen production of the WHR-ORC-P2G system is formulated as follows:

$$\begin{cases} P_t^{\mathrm{H_2,EL}} = \eta_{\mathrm{EL}}P_t^{\mathrm{e,EL}} \\ P_t^{\mathrm{O_2,EL}} = 0.5P_t^{\mathrm{H_2,EL}} \\ P_{\min}^{\mathrm{e,EL}} \le P_t^{\mathrm{e,EL}} \le P_{\max}^{\mathrm{e,EL}}, \end{cases} \tag{9}$$

where $P_t^{\mathrm{e,EL}}$, $P_{\mathrm{EL},t}^{\mathrm{H_2}}$, and $P_t^{\mathrm{O_2,EL}}$ denote the electrical power input, hydrogen power output, and oxygen power output of the EL, respectively; η_{EL} denotes the hydrogen production coefficient; and $P_{\max}^{\mathrm{e,EL}}$ and $P_{\min}^{\mathrm{e,EL}}$ denote the maximum and minimum electrical power inputs of the EL, respectively.

Furthermore, waste heat recovery and power generation during the P2G energy conversion process are achieved through the WHR and ORC processes. The hydrogen fuel cell (HFC) and methanation reactor (MR) are also incorporated into the P2G subsystem for coordinated hydrogen utilization and energy conversion. Accordingly, the thermal and electrical output models of the improved P2G system are formulated as follows:

$$\begin{cases} P_t^{\mathrm{h,HFC}} = P_{t,\mathrm{WHB}}^{\mathrm{h,HFC}} + P_{t,\mathrm{ORC}}^{\mathrm{h,HFC}} \\ P_t^{\mathrm{h,MR}} = P_{t,\mathrm{WHB}}^{\mathrm{h,MR}} + P_{t,\mathrm{ORC}}^{\mathrm{h,MR}} \\ P_t^{\mathrm{h,MR}} = \eta_{\mathrm{MR}}^{\mathrm{h}}P_t^{\mathrm{g,MR}} \\ P_t^{\mathrm{g,MR}} = \eta_{\mathrm{MR}}^{\mathrm{H_2}}P_t^{\mathrm{H_2,MR}} \\ k_{\min}^{\mathrm{HFC}}P_t^{\mathrm{e,HFC}} \le P_t^{\mathrm{h,HFC}} \le k_{\max}^{\mathrm{HFC}}P_t^{\mathrm{e,HFC}} \\ P_t^{\mathrm{e,HFC}} = \eta_{\mathrm{HFC}}^{\mathrm{e}}P_t^{\mathrm{H_2,HFC}} \\ P_{\min}^{\mathrm{H_2,HFC}} \le P_t^{\mathrm{H_2,HFC}} \le P_{\max}^{\mathrm{H_2,HFC}} \\ P_{\min}^{\mathrm{H_2,MR}} \le P_t^{\mathrm{H_2,MR}} \le P_{\max}^{\mathrm{H_2,MR}} \\ \left|P_t^{\mathrm{H_2,HFC}} - P_{t-1}^{\mathrm{H_2,HFC}}\right| \le R_{\max}^{\mathrm{H_2,HFC}} \\ \left|P_t^{\mathrm{H_2,MR}} - P_{t-1}^{\mathrm{H_2,MR}}\right| \le R_{\max}^{\mathrm{H_2,MR}}, \end{cases} \tag{10}$$

where $P_{t,\mathrm{WHB}}^{\mathrm{h,HFC}}$ and $P_{t,\mathrm{WHB}}^{\mathrm{h,MR}}$ denote the thermal powers delivered from the HFC and MR to the WHB, respectively; $P_{t,\mathrm{ORC}}^{\mathrm{h,HFC}}$ and $P_{t,\mathrm{ORC}}^{\mathrm{h,MR}}$ denote the thermal powers delivered from the HFC and MR to the ORC process respectively; $P_t^{\mathrm{h,HFC}}$ and $P_t^{\mathrm{h,MR}}$ denote the thermal power outputs of the HFC and MR, respectively; $P_t^{\mathrm{g,MR}}$ denotes the gas power output of the MR; $\eta_{\mathrm{MR}}^{\mathrm{h}}$ and $\eta_{\mathrm{MR}}^{\mathrm{H_2}}$ denote the heat production coefficient and hydrogen-to-gas conversion efficiency of the MR, respectively; $\eta_{\mathrm{HFC}}^{\mathrm{e}}$, $k_{\min}^{\mathrm{HFC}}$, and $k_{\max}^{\mathrm{HFC}}$ denote the electricity generation efficiency and the minimum and maximum heat-to-power ratios of the HFC, respectively; $P_t^{\mathrm{H_2,HFC}}$, $P_{\min}^{\mathrm{H_2,HFC}}$, and $P_{\max}^{\mathrm{H_2,HFC}}$ denote the hydrogen input and its minimum and maximum limits for the HFC, respectively; $P_t^{\mathrm{H_2,MR}}$, $P_{\min}^{\mathrm{H_2,MR}}$, and $P_{\max}^{\mathrm{H_2,MR}}$ denote the hydrogen input power and its minimum and maximum limits of the MR, respectively; and $R_{\max}^{\mathrm{H_2,HFC}}$ and $R_{\max}^{\mathrm{H_2,HFC}}$ denote the maximum ramping limits of the hydrogen input powers of the HFC and MR, respectively.

The ORC and WHR outputs within the WHR-ORC-P2G system should satisfy

$$\begin{cases} P_t^{\mathrm{h,WHB}} = \eta_{\mathrm{WHB}}(P_{t,\mathrm{WHB}}^{\mathrm{h,HFC}} + P_{t,\mathrm{WHB}}^{\mathrm{h,MR}}) \\ P_t^{\mathrm{e,ORC}} = \eta_{\mathrm{ORC}}(P_{t,\mathrm{ORC}}^{\mathrm{h,HFC}} + P_{t,\mathrm{ORC}}^{\mathrm{h,MR}}), \end{cases} \tag{11}$$

where η_{WHB} and η_{ORC} denote the thermal recovery efficiency of the WHR and the power generation efficiency of the ORC process in the WHR-ORC-P2G system, respectively, and $P_t^{\mathrm{h,WHB}}$ and $P_t^{\mathrm{e,ORC}}$ denote the thermal power output of the WHR and the electrical power output of the ORC process, respectively.

3. DGCACTM and MDRM

The DGCACTM and MDRM are incorporated into the proposed HACP-IES dispatch framework to optimize the energy-use structure of the HACP-IES and exploit demand-side flexibility. The DGCACTM coordinates the GC market and CT market to guide green electricity consumption and carbon emission behavior through market-based incentives and penalties, while the MDRM facilitates peak shaving, valley filling, and multi-energy substitution on the use side in the system. Through their coordinated effects, renewable energy accommodation is enhanced while the overall operating cost and carbon emissions of the HACP-IES are reduced.

3.1. DGCACTM

The GC and carbon trading (CT) markets are important market-based mechanisms for promoting renewable electricity utilization and carbon emission reduction in modern power systems [31–34]. Existing studies on GC and CT generally adopt a daily settlement time scale and assume fixed trading prices, neglecting the dynamic relationships among market supply and demand, trading volumes, and real-time prices at finer time scales. Consequently, they cannot accurately capture the actual market characteristics of real-time GC trading and CT. Accordingly, a DGCACTM is proposed in this work. According to market economic principles, considering market demand elasticity and price feedback, the trading prices of GCs and carbon allowances during CT are closely related to their real-time selling volumes [32], while real-time market saturation points should also be considered. Specifically, when the traded number of GCs or carbon allowances is relatively small, market demand remains unmet, and additional supply can generate rapidly increasing revenues. As transactions expand, demand gradually approaches saturation, causing the benefit of further sales to decline. Once the traded amount exceeds a certain threshold, the market becomes nearly saturated, and additional transactions provide only limited incremental revenue. Based on the above characteristics, a piecewise revenue function is used in the proposed DGCACTM to characterize the dynamic nonlinear relationship between the selling volumes of GCs and carbon allowances and the corresponding trading revenues. Accordingly, to characterize the nonlinear relationship between transaction volumes and the

corresponding revenues of the IES in the GC and CT markets, the trading revenue functions under the proposed DGCACTM are formulated as follows:

$$f_{\mathrm{GC/CT}} = \begin{cases} a^{\mathrm{GC/CT}}\left(Q_{t,\mathrm{tre}}^{\mathrm{GC/CT}}\right)^2 + b^{\mathrm{GC/CT}} Q_{t,\mathrm{tre}}^{\mathrm{GC/CT}} + C_{\mathrm{base}}^{\mathrm{GC/CT}} \\ 0 \le Q_{t,\mathrm{tre}}^{\mathrm{GC/CT}} \le Q_{\mathrm{max,tre}}^{\mathrm{GC/CT}} \\ C_{\mathrm{max}}^{\mathrm{GC/CT}}, Q_{t,\mathrm{tre}}^{\mathrm{GC/CT}} \ge Q_{\mathrm{max,tre}}^{\mathrm{GC/CT}} \\ -a^{\mathrm{GC/CT}}\left(Q_{t,\mathrm{tre}}^{\mathrm{GC/CT}}\right)^2 + b^{\mathrm{GC/CT}} Q_{t,\mathrm{tre}}^{\mathrm{GC/CT}} - C_{\mathrm{base}}^{\mathrm{GC/CT}} \\ -Q_{\mathrm{max,tre}}^{\mathrm{GC/CT}} \le Q_{t,\mathrm{tre}}^{\mathrm{GC/CT}} \le 0 \\ -C_{\mathrm{max}}^{\mathrm{GC/CT}}, -Q_{\mathrm{max,tre}}^{\mathrm{GC/CT}} \ge Q_{t,\mathrm{tre}}^{\mathrm{GC/CT}}, \end{cases} \tag{12}$$

where $f_t^{\mathrm{GC/CT}}$ denotes the dynamic cost function of the GC/CT market, $a^{\mathrm{GC/CT}}$ and $b^{\mathrm{GC/CT}}$ are the function coefficients, and $Q_{\mathrm{max,tre}}^{\mathrm{GC/CT}}$ and $Q_{t,\mathrm{tre}}^{\mathrm{GC/CT}}$ denote the dynamic trading saturation point and the real-time trading volume of GCs/carbon allowances, respectively.

The joint trading process of the DGCACTM is illustrated in Figure 3. Under the GCM, the HACP-IES receives GCs in proportion to its green electricity generation, which can subsequently be traded in the market. The system is required to satisfy a prescribed GC quota: surplus GCs can be sold to generate GC revenue, whereas any deficit must be covered through additional purchases. Accordingly, the GC trading cost for the HACP-IES is formulated as follows:

$$\begin{cases} Q_{t,\mathrm{s}}^{\mathrm{GC}} = \beta_{\mathrm{GC}} P_t^{\mathrm{e,load}} \\ Q_{t,\mathrm{d}}^{\mathrm{GC}} = \alpha_{\mathrm{GC}} P_t^{\mathrm{e,WT}} \\ Q_{t,\mathrm{tre}}^{\mathrm{GC}} = Q_{t,\mathrm{s}}^{\mathrm{GC}} - Q_{t,\mathrm{d}}^{\mathrm{GC}}, \end{cases} \tag{13}$$

where β_{GC} and α_{GC} denote the GC quota coefficient and the GC conversion coefficient for the system, respectively, and $Q_{t,\mathrm{s}}^{\mathrm{GC}}$ and $Q_{t,\mathrm{d}}^{\mathrm{GC}}$ denote the GC quota and the number of obtained GCs for the HACP-IES, respectively.

$$\begin{cases} Q_{t,\mathrm{s}}^{\mathrm{CT}} = \beta_{\mathrm{CT}}^{\mathrm{GB}} P_t^{\mathrm{h,GB}} + \beta_{\mathrm{CT}}^{\mathrm{grid}} P_t^{\mathrm{e,grid}} + \sum_{i=1}^{N_{\mathrm{w}}} \beta_{\mathrm{CT}}^{\mathrm{h,WCHPU}} P_{i,t}^{\mathrm{h,WCHPU}} + \beta_{\mathrm{CT}}^{\mathrm{e,WCHPU}} P_{i,t}^{\mathrm{e,WCHPU}} \\ Q_{t,\mathrm{d}}^{\mathrm{CT}} = \alpha_{\mathrm{CT}}^{\mathrm{GB}} P_t^{\mathrm{h,GB}} + \alpha_{\mathrm{CT}}^{\mathrm{grid}} P_t^{\mathrm{e,grid}} + \sum_{i=1}^{N_{\mathrm{w}}} \alpha_{\mathrm{CT}}^{\mathrm{h,WCHPU}} P_{i,t}^{\mathrm{h,WCHPU}} + \alpha_{\mathrm{CT}}^{\mathrm{e,WCHPU}} P_{i,t}^{\mathrm{e,WCHPU}} \alpha_{\mathrm{CT}}^{\mathrm{CSS}} P_{i,t}^{\mathrm{e,CCS}} \\ Q_{t,\mathrm{GC}}^{\mathrm{CT}} = \beta_{\mathrm{GC}} Q_{t,\mathrm{s}}^{\mathrm{GC}} \\ Q_{t,\mathrm{MR}}^{\mathrm{CT}} = \beta_{\mathrm{MR}}^{\mathrm{CO_2}} P_t^{\mathrm{g,MR}} \\ Q_{t,\mathrm{tre}}^{\mathrm{CT}} = Q_{t,\mathrm{s}}^{\mathrm{CT}} - \left(Q_{t,\mathrm{d}}^{\mathrm{CT}} - Q_{t,\mathrm{GC}}^{\mathrm{CT}} - Q_{t,\mathrm{MR}}^{\mathrm{CT}}\right), \end{cases} \tag{14}$$

where $\beta_{\mathrm{CT}}^{\mathrm{GB}}$, $\beta_{\mathrm{CT}}^{\mathrm{grid}}$, $\beta_{\mathrm{CT}}^{\mathrm{h,WCHPU}}$ and $\beta_{\mathrm{CT}}^{\mathrm{e,WCHPU}}$ denote the carbon allowance coefficients of the corresponding devices, respectively; $\alpha_{\mathrm{CT}}^{\mathrm{GB}}$, $\alpha_{\mathrm{CT}}^{\mathrm{grid}}$, $\alpha_{\mathrm{CT}}^{\mathrm{h,WCHPU}}$ and $\alpha_{\mathrm{CT}}^{\mathrm{e,WCHPU}}$ denote the carbon emission coefficients of the corresponding devices, respectively; $\alpha_{\mathrm{CT}}^{\mathrm{CSS}}$ denotes the amount of CO_2 captured by the CCS system; β_{GC} denotes the carbon-offset coefficient of GCs; $Q_{t,\mathrm{s}}^{\mathrm{GC}}$, $Q_{t,\mathrm{d}}^{\mathrm{GC}}$ and $Q_{t,\mathrm{GC}}^{\mathrm{CT}}$ denote the carbon allowance, actual carbon emissions, and carbon emissions offset by the GCs of the HACP-IES, respectively.

Finally, the total GC trading and CT costs of the HACP-IES are formulated as follows:

$$\begin{cases} \dot{f}_{\mathrm{GC}} = \sum_{t=1}^{T} f_{\mathrm{GC}}(Q_{t,\mathrm{tre}}^{\mathrm{GC}}) \\ \dot{f}_{\mathrm{CT}} = \sum_{t=1}^{T} f_{\mathrm{CT}}(Q_{t,\mathrm{tre}}^{\mathrm{CT}}), \end{cases} \tag{15}$$

where $\dot{f}_{\mathrm{GC}}$ and $\dot{f}_{\mathrm{CT}}$ denote the total GC trading cost and CT cost of the system, respectively.

In summary, the proposed DGCACTM can more accurately characterize the nonlinear relationship between the trading volumes of GCs and carbon allowances and their corresponding revenues at finer temporal resolutions, thereby enhancing the temporal granularity and dynamic representation of market transactions in the dispatch model.

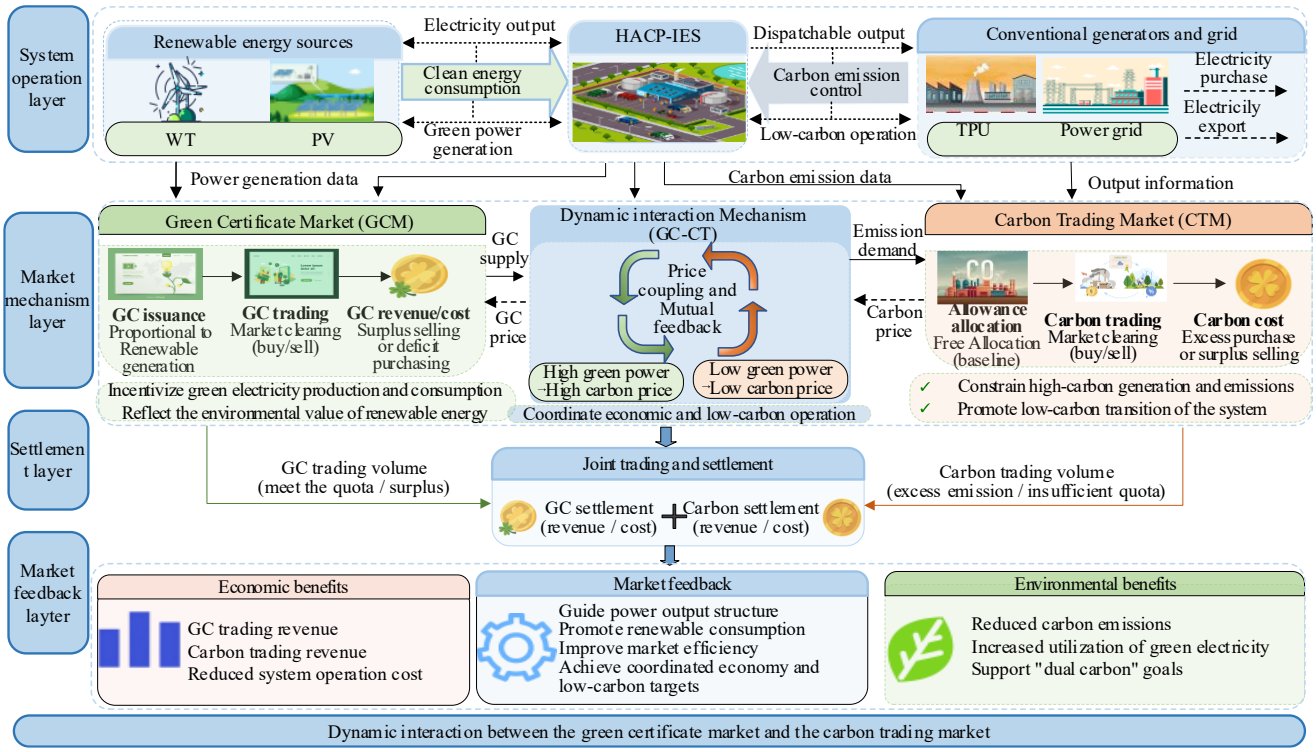

Figure 3. Interactive regulation mechanism of GC and carbon trading.

3.2. Multi-Energy Demand Response Mechanism

The HACP-IES accommodates various energy demands, including electricity, heat, gas, and oxygen. To improve demand-side flexibility and energy-use efficiency, an MDRM is introduced. Since the oxygen demand is directly associated with personnel safety, it is not included in the MDRM.

According to the load characteristics of electrical, thermal, and gas demands, the loads in the HACP-IES are categorized as fixed, shiftable, and substitutable loads. Fixed loads remain unchanged and are therefore excluded from demand response. Shiftable loads, in contrast, can be redistributed across different time periods in response to scheduling signals, while their total energy consumption over the entire response horizon remains constant. The shiftable load for the system is formulated as follows:

$$\begin{cases} P_{t,\mathrm{s}}^{i,\mathrm{load}} = P_{t,\mathrm{s,ini}}^{i,\mathrm{load}} + \Delta P_{t,\mathrm{s}}^{i,\mathrm{load}} \\ \Delta P_{t,\mathrm{s}}^{i,\mathrm{load}} = P_{t,\mathrm{in,s}}^{i,\mathrm{load}} - P_{t,\mathrm{out,s}}^{i,\mathrm{load}} \\ 0 \le P_{t,\mathrm{in,s}}^{i,\mathrm{load}} \le x_{t,\mathrm{s}}^{i,\mathrm{in}} P_{\mathrm{max,in,s}}^{i,\mathrm{load}} \\ 0 \le P_{t,\mathrm{out,s}}^{i,\mathrm{load}} \le x_{t,\mathrm{s}}^{i,\mathrm{out}} P_{\mathrm{max,out,s}}^{i,\mathrm{load}} \\ x_{t,\mathrm{s}}^{i,\mathrm{in}} + x_{t,\mathrm{s}}^{i,\mathrm{out}} \le 1 \\ \sum_{t=1}^{T} \Delta P_{t,\mathrm{s}}^{i,\mathrm{load}} = 0 \\ i \in \Omega_{\mathrm{load}} = \{\mathrm{e,h,g}\} \end{cases} \tag{16}$$

where $P_{t,\mathrm{s}}^{i,\mathrm{load}}$, $P_{t,\mathrm{s,ini}}^{i,\mathrm{load}}$, and $\Delta P_{t,\mathrm{s}}^{i,\mathrm{load}}$ denote the i-th power of the shiftable load after demand response, the power before demand response, and the shifted power, respectively; $P_{t,\mathrm{in,s}}^{i,\mathrm{load}}$ and $P_{t,\mathrm{out,s}}^{i,\mathrm{load}}$ denote the shifted-in and shifted-out powers of the i-th shiftable load, respectively; $x_{t,\mathrm{s}}^{i,\mathrm{in}}$ and $x_{t,\mathrm{s}}^{i,\mathrm{out}}$ denote the binary state variables associated with the shifted-in and shifted-out states of the i-th shiftable load, respectively; $P_{\mathrm{max,in,s}}^{i,\mathrm{load}}$ and $P_{\mathrm{max,out,s}}^{i,\mathrm{load}}$ denote the maximum shifted-in and shifted-out powers of the i-th shiftable load, respectively; Ω_{load} denotes the set of loads participating in demand response.

The substitutable load for the system can be expressed as follows:

$$\begin{cases} P_{t,\mathrm{c}}^{i,\mathrm{load}} = P_{t,\mathrm{c,ini}}^{i,\mathrm{load}} + \Delta P_{t,\mathrm{c}}^{i,\mathrm{load}} \\ P_{t,\mathrm{c}}^{i,\mathrm{load}} = P_{t,\mathrm{in,c}}^{i,\mathrm{load}} - P_{t,\mathrm{out,c}}^{i,\mathrm{load}} \\ 0 \le P_{t,\mathrm{in,c}}^{i,\mathrm{load}} \le x_{t,\mathrm{c}}^{i,\mathrm{in}} P_{\mathrm{max,in,c}}^{i,\mathrm{load}} \\ 0 \le P_{t,\mathrm{out,c}}^{i,\mathrm{load}} \le x_{t,\mathrm{c}}^{i,\mathrm{out}} P_{\mathrm{max,out,c}}^{i,\mathrm{load}} \\ x_{t,\mathrm{c}}^{i,\mathrm{in}} + x_{t,\mathrm{c}}^{i,\mathrm{out}} = 1 \\ \sum\limits_{i \in \Omega_{\mathrm{load}}} \Delta P_{t,\mathrm{c}}^{i,\mathrm{load}} = 0 \end{cases} \tag{17}$$

where $P_{t,\mathrm{c}}^{i,\mathrm{load}}$, $P_{t,\mathrm{c,ini}}^{i,\mathrm{load}}$, and $\Delta P_{t,\mathrm{c}}^{i,\mathrm{load}}$ denote the power of the i-th substitutable load after demand response, the power before demand response, and the substituted power, respectively; $P_{t,\mathrm{in,s}}^{i,\mathrm{load}}$ and $P_{t,\mathrm{out,s}}^{i,\mathrm{load}}$ denote the transferred-in and transferred-out powers of the i-th substitutable load, respectively; $x_{t,\mathrm{s}}^{i,\mathrm{in}}$ and $x_{t,\mathrm{s}}^{i,\mathrm{out}}$ are the binary state variables associated with the transferred-in and transferred-out powers of the i-th substitutable load, respectively; $P_{\mathrm{max,in,c}}^{i,\mathrm{load}}$ and $P_{\mathrm{max,out,c}}^{i,\mathrm{load}}$ denote the maximum transferred-in and transferred-out powers of the i-th substitutable load, respectively.

To ensure energy conservation during cross-carrier demand substitution, an equivalent energy balance constraint is introduced by considering the conversion efficiencies of the EB and GB. The constraint ensures that the original useful heating demand is maintained despite changes in electricity, heat, and gas consumption. Meanwhile, the substitutable load ratio and the corresponding adjustment limits restrict the extent of energy substitution, while equipment capacity constraints ensure the availability of alternative energy supplies.

$$\begin{cases} \eta_{\mathrm{EB}} \Delta P_{t,\mathrm{c}}^{\mathrm{e,load}} + \Delta P_{t,\mathrm{c}}^{\mathrm{h,load}} + \eta_{\mathrm{GB}} \Delta P_{t,\mathrm{c}}^{\mathrm{g,load}} = 0 \\ 0 \le P_{t,\mathrm{out,c}}^{i,\mathrm{load}} \le x_{t,\mathrm{c}}^{i,\mathrm{out}} \min\left\{ P_{\mathrm{max,out,c}}^{i,\mathrm{load}}, \alpha_i P_{t,\mathrm{ini,c}}^{i,\mathrm{load}} \right\} \\ 0 \le P_{t,\mathrm{in},c}^{i,\mathrm{load}} \le x_{t,c}^{i,\mathrm{in}} P_{\mathrm{max,in,c}}^{i,\mathrm{load}}, \quad i \in \{\mathrm{e,h,g}\} \end{cases} \tag{18}$$

4. Dispatch Optimization Model and Solution Method

4.1. Objective Function

To achieve the cost-effective and low-carbon operation of the HACP-IES, an optimal dispatch model for the HACP-IES is formulated by integrating energy curtailment, system operation, GC trading, CT, and demand response costs into the objective function, which is given as follows:

$$\min f = \min(f_{\mathrm{ab}} + f_{\mathrm{m}} + f_{\mathrm{buy}} + \dot{f}_{\mathrm{GC}} + \dot{f}_{\mathrm{CT}} + f_{\mathrm{DR}}), \tag{19}$$

where f_{ab} denotes the system energy curtailment cost, f_{m} denotes the system operating cost, f_{buy} denotes the system energy purchase cost, and f_{DR} denotes the system demand response cost.

4.1.1. Energy Curtailment Cost

$$f_{\mathrm{ab}} = c_{\mathrm{ab}}^{\mathrm{WT}} \sum_{t=1}^{T} (\hat{P}_t^{\mathrm{e,WT}} - P_t^{\mathrm{e,WT}}) + c_{\mathrm{ab}}^{\mathrm{PV}} \sum_{t=1}^{T} (\hat{P}_t^{\mathrm{e,PV}} - P_t^{\mathrm{e,PV}}), \tag{20}$$

where $c_{\mathrm{ab}}^{\mathrm{WT}}$ and $c_{\mathrm{ab}}^{\mathrm{PV}}$ denote the wind and photovoltaic electricity curtailment cost coefficients, respectively; $\hat{P}_t^{\mathrm{e,WT}}$ and $\hat{P}_t^{\mathrm{e,PV}}$ denote the forecasted wind and photovoltaic electricity outputs, respectively.

4.1.2. Energy Purchase Cost

$$f_{\mathrm{buy}} = \sum_{t=1}^{T} (c_t^{\mathrm{grid}} P_t^{\mathrm{e,grid}} + c_t^{\mathrm{gas}} P_t^{\mathrm{g,net}}) \Delta t, \tag{21}$$

where c_t^{grid} and c_t^{gas} denote the electricity price and gas price for the system, respectively; $P_t^{\text{e,grid}}$ and $P_t^{\text{g,net}}$ denote the purchased electricity and gas quantities, respectively.

4.1.3. Operating Cost

$$f_{\text{m}} = \sum_{i \in \Omega_{\text{all}}} \sum_{j \in \Omega_{\text{power}}} \sum_{t=1}^{T} c_i P_t^{j,i} \Delta t \,, \tag{22}$$

where c_i denotes the operation and maintenance cost coefficient of the corresponding device, $P_t^{j,i}$ denotes the type-j power output of the corresponding device i, and Ω_{all} and Ω_{power} denote the sets of devices and output types within the HACP-IES, respectively.

4.1.4. Demand Response Cost

$$f_{\text{DR}} = \sum_{i \in \Omega_{\text{load}}} \sum_{t=1}^{T} c_{\text{s}}^{\text{load}} \left(P_{t,\text{in,s}}^{i,\text{load}} + P_{t,\text{out,s}}^{i,\text{load}} \right) + c_{\text{c}}^{\text{load}} (P_{t,\text{in,c}}^{i,\text{load}} + P_{t,\text{out,c}}^{i,\text{load}}) \,, \tag{23}$$

where $c_{\text{s}}^{\text{load}}$ and $c_{\text{c}}^{\text{load}}$ denote the cost coefficients of shiftable and substitutable loads participating in demand response, respectively.

4.2. Constraints

4.2.1. Operational Constraints of Energy Storage Devices

In addition to the key device models described above, the HACP-IES also includes multiple energy storage devices for electricity, heat, gas, hydrogen, and oxygen, with their operational constraints expressed as follows:

$$\begin{cases} 0 \le P_{t,\text{cha}}^{i,\text{ES}} \le \zeta_{t,\text{cha}}^{i,\text{ES}} P_{\text{max,cha}}^{i,\text{ES}} \\ 0 \le P_{t,\text{dis}}^{i,\text{ES}} \le \zeta_{t,\text{dis}}^{i,\text{ES}} P_{\text{max,dis}}^{i,\text{ES}} \\ S_t^{i,\text{ES}} = S_{t-1}^{i,\text{ES}} + P_{t,\text{dis}}^{i,\text{ES}} \eta_{\text{dis}}^{i,\text{EC}} - P_{t,\text{cha}}^{i,\text{ES}} / \eta_{\text{cha}}^{i,\text{ES}} \\ S_1^{i,\text{ES}} = S_T^{i,\text{ES}} \\ \zeta_{t,\text{cha}}^{i,\text{ES}} + \zeta_{t,\text{dis}}^{i,\text{ES}} \le 1 \\ S_{\text{min}}^{i,\text{ES}} \le S_t^{i,\text{ES}} \le S_{\text{max}}^{i,\text{ES}} \\ i \in \{\text{e, h, g, } \text{O}_2\text{, } \text{H}_2\}, \end{cases} \tag{24}$$

where $P_{t,\text{cha}}^{i,\text{ES}}$ and $P_{t,\text{dis}}^{i,\text{ES}}$ denote the charging and discharging powers of the corresponding energy storage device, respectively; $P_{\text{max,cha}}^{i,\text{ES}}$ and $P_{\text{max,dis}}^{i,\text{ES}}$ denote the maximum charging and discharging powers of the corresponding energy storage device, respectively; $\zeta_{t,\text{cha}}^{i,\text{ES}}$ and $\zeta_{t,\text{dis}}^{i,\text{ES}}$ denote the binary charging and discharging state variables of the corresponding energy storage device, respectively; $\eta_{\text{dis}}^{i,\text{EC}}$ and $\eta_{\text{cha}}^{i,\text{ES}}$ denote the discharging and charging efficiencies of the corresponding energy storage device, respectively; $S_t^{i,\text{ES}}$ denotes the stored energy of the corresponding energy storage device; $S_{\text{max}}^{i,\text{ES}}$ and $S_{\text{min}}^{i,\text{ES}}$ denote the maximum and minimum stored energy of the corresponding energy storage device, respectively.

4.2.2. Power Balance Constraints

Furthermore, the power balance of the system should also be considered.

$$\begin{cases} P_t^{\text{e,WT}} + P_t^{\text{e,PV}} + P_t^{\text{e,HFC}} + P_{t,\text{dis}}^{\text{e,ES}} + P_t^{\text{e,grid}} + \sum_{i=1}^{N_{\text{w}}} P_{i,t}^{\text{e,WCHPU}} \\ + P_t^{\text{e,ORC}} = P_{t,\text{DR}}^{\text{e,load}} + P_t^{\text{e,EL}} + P_t^{\text{e,EB}} + P_{t,\text{cha}}^{\text{e,ES}} + P_t^{\text{e,VPSAU}} \\ P_t^{\text{h,GB}} + P_{t,\text{dis}}^{\text{h,ES}} + P_t^{\text{h,WHB}} + \sum_{i=1}^{N_{\text{w}}} P_{i,t}^{\text{h,WCHPU}} = P_{t,\text{DR}}^{\text{h,load}} + P_{t,\text{cha}}^{\text{h,ES}} \\ P_t^{\text{g,MR}} + P_t^{\text{g,net}} + P_{t,\text{dis}}^{\text{g,ES}} = P_{t,\text{DR}}^{\text{g,load}} + P_{t,\text{cha}}^{\text{g,ES}} + P_t^{\text{g,GB}} \\ P_t^{\text{H}_2\text{,EL}} + P_{t,\text{dis}}^{\text{H}_2\text{,ES}} = P_t^{\text{H}_2\text{,MR}} + P_t^{\text{H}_2\text{,HFC}} + P_{t,\text{cha}}^{\text{H}_2\text{,ES}} \\ P_t^{\text{O}_2\text{,EL}} + P_t^{\text{O}_2\text{,VPSAU}} + P_{t,\text{dis}}^{\text{O}_2\text{,ES}} = P_t^{\text{O}_2\text{,load}} + P_{t,\text{cha}}^{\text{O}_2\text{,ES}}, \end{cases} \tag{25}$$

where $P_{t,\mathrm{DR}}^{\mathrm{e,load}}$, $P_{t,\mathrm{DR}}^{\mathrm{h,load}}$, and $P_{t,\mathrm{DR}}^{\mathrm{g,load}}$ denote the electrical, thermal, and gas loads after demand response, respectively; $P_t^{\mathrm{O_2,load}}$ denotes the oxygen load power; $P_t^{\mathrm{h,GB}}$ and $P_t^{\mathrm{g,GB}}$ denote the thermal power output and gas power input of the GB, respectively; $P_t^{\mathrm{e,VPSAU}}$ and $P_t^{\mathrm{O_2,VPSAU}}$ denote the electrical power input and oxygen power output of the VPSAU, respectively.

4.2.3. Wind and Photovoltaic Power Uncertainty Constraints

Wind and photovoltaic generation in the HACP-IES are subject to forecasting uncertainties, which may affect system operational reliability. To address these uncertainties, a chance-constrained optimization approach is adopted based on the probabilistic characteristics of renewable generation forecasting errors [35–37]. Following the normal distribution assumptions employed in related studies [36,37], the wind and photovoltaic forecasting errors are assumed to follow zero-mean normal distributions with corresponding variances. Furthermore, the confidence level is set to 0.95, consistent with previous chance-constrained dispatch studies [35,36], to balance operational reliability and economic performance. Under this assumption, the corresponding one-sided standard normal quantile is 1.645. Let $F(\cdot)$ and $F^{-1}(\cdot)$ denote the cumulative distribution function of the standard normal distribution and its inverse, respectively. Accordingly, the probabilistic reserve requirements associated with electrical power balance can be reformulated as follows:

$$\begin{aligned} &P_t^{\mathrm{e,WT}} + P_t^{\mathrm{e,PV}} + P_t^{\mathrm{e,grid}} + P_t^{\mathrm{e,WCHPU}} + P_t^{\mathrm{e,HFC}} + P_{t,\mathrm{dis}}^{\mathrm{e,ES}} + P_t^{\mathrm{e,ORC}} \geq \\ &P_{\mathrm{DR},t}^{\mathrm{e,load}} + P_t^{\mathrm{e,VPSAU}} + P_t^{\mathrm{e,EL}} + P_{\mathrm{EB},t}^{\mathrm{e}} + P_{t,\mathrm{cha}}^{\mathrm{e,ES}} + F^{-1}(\alpha)\sqrt{\sigma_{\mathrm{WT}}^2 + \sigma_{\mathrm{PV}}^2}, \end{aligned} \tag{26}$$

where $F^{-1}(\alpha)$ denotes the inverse cumulative distribution function of the standard normal distribution, and $\sigma_{\mathrm{WT/PV}}^2$ denotes the variance of the WT/PV power output.

4.3. Solution Method

Considering the objective function and operational constraints described above, the HACP-IES dispatch model is formulated as a mixed-integer nonlinear programming problem. To enable an efficient solution with a commercial solver, the nonlinear terms are transformed into linear forms through piecewise linear approximation. Assuming that the nonlinear function is partitioned into N subintervals, its linearized representation can be expressed by the following constraints:

$$\begin{cases} \gamma_1 + \gamma_2 + \cdots + \gamma_{N+1} = 1 \\ \beta_1 + \beta_2 + \cdots + \beta_N = 1 \\ 0 \leqslant \gamma_j, \quad j = 1, 2, \ldots, N+1 \\ \gamma_1 \leqslant \beta_1, \gamma_2 \leqslant \beta_1 + \beta_2, \ldots, \gamma_{N+1} \leqslant \beta_N \\ x = \sum_{j=1}^{N+1} \alpha_j \gamma_j, f(x) = \sum_{j=1}^{N+1} f(\alpha_j)\gamma_j, \end{cases} \tag{27}$$

where β_j and γ_j denote the binary and continuous auxiliary variables introduced for piecewise linearization, respectively, and α_j and $f(\alpha_j)$ denote the breakpoints of the independent and dependent variables of the function, respectively.

The solution procedure comprises parameter initialization, device and market modeling, piecewise linearization, and optimization. The model minimizes total system operating cost subject to device operating constraints, multi-energy balances, demand response constraints, and uncertainty-related constraints. Scenario 8 additionally incorporates actual carbon emissions through a normalized linear weighted objective.

Equation (27) is specifically applied to the nonlinear GC and CT transaction cost functions defined in Equation (12). Each function is represented by 20 uniformly spaced nodes, yielding 19 linear segments over −40 to 40 certificates for GC trading and −20 to 20 t for CT. Binary variables represent operating modes and state transitions and are linked

to continuous dispatch variables through linear capacity bounds and logical constraints. The remaining device equations, energy balances, and deterministic uncertainty constraints are linear. Consequently, the resulting formulation is a mixed-integer linear programming (MILP) model with SOS2 constraints.

The model is implemented in MATLAB R2022a using YALMIP R20250626 and GUROBI 10.0.1. The relative MIP-gap tolerance is set to 3%. The complete solution procedure is illustrated in Figure 4.

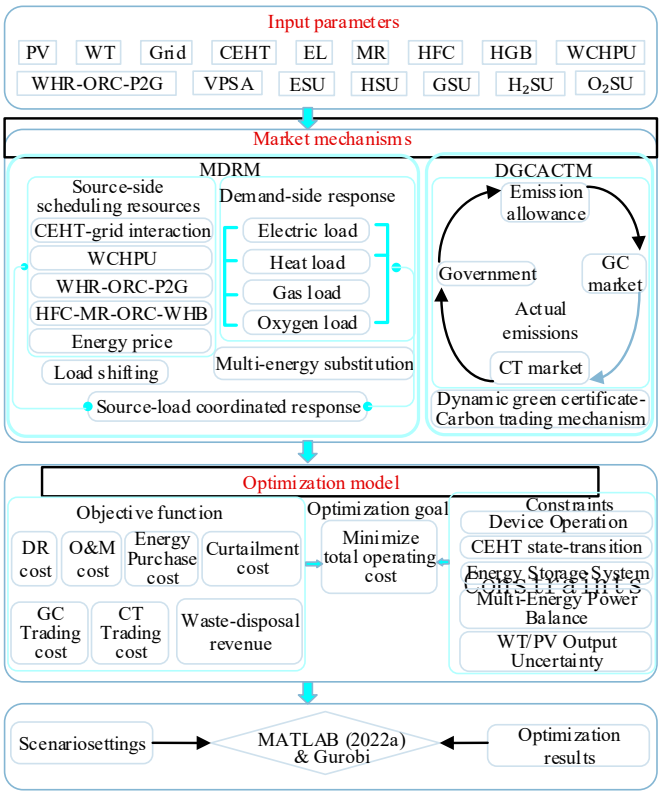

Figure 4. Flowchart of proposed HACP-IES scheduling method.

5. Case Study Analysis

5.1. Case Study Overview

To verify the effectiveness of the proposed method, a case study is carried out using the forecasted wind and photovoltaic generation and load data of a construction park. The detailed input data are provided in Figure 5.

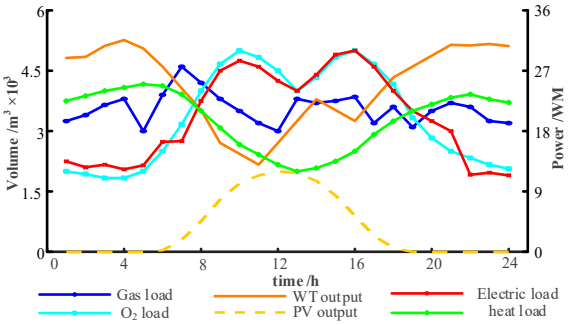

Figure 5. Case study data.

The main energy conversion relationships of the HACP-IES devices are summarized in Table 1. The EL converts electricity into hydrogen and oxygen, whereas the MR converts hydrogen into gas. The HFC utilizes hydrogen to generate electricity and heat, with conversion coefficients of 1.70 and 1.20, respectively. The GB and EB provide heat through gas combustion and electrical heating, respectively. In addition, the VPSAU and ASU consume electricity to produce oxygen, while the WCHPU converts construction waste into electricity and heat. The ORC recovers waste heat for power generation. The conversion coefficients are defined according to the corresponding input–output relationships in the device models, with their physical meanings and units determined by the associated variables. In particular, the HFC coefficients are specified according to the conversion equations in the model rather than being directly interpreted as dimensionless efficiencies.

Table 1. Parameters of energy conversion equipment.

Equipment	Power Limit (MW)	Energy Type	Conversion Coefficient/Efficacy	Ramp Rate (%)
EL	15	Electrical input	0.75 (electricity → H_2) 0.375 (electricity → O_2)	25
MR	5	Hydrogen input	0.60 (H_2 → gas)	20
HFC	5	Hydrogen input	1.70 (H_2 → electricity) 1.20 (H_2 → heat)	20
GB	60	Thermal output	λ_G = 10 (gas →heat)	25
EB	2	Electrical input	0.83 (electricity → heat)	25
VPSAU	5	Electrical input	$Pe = 0.70P_{O2}$	25
ASU	2	Electrical input	$Pe = 0.60P_{O2}$	25
WCHPU	6	Thermal and electrical output	1.10 (waste → electricity) 0.80 (waste → heat) heat-to-power ratio: 0.50–1.10	25
ORC	—	Heat input	0.30 (heat → electricity)	—
WHB	—	Recovered heat	—	—

The scenario configurations are listed in Table 2. Scenario 1 is adopted as the benchmark case. Building on this basis, Scenario 2 adds the proposed WHR-ORC-P2G system to assess its contribution, while Scenario 3 further considers CEHT–grid interaction to quantify the economic benefits of CEHTs participating in system dispatch. Scenario 4 considers only the function of the GC mechanism, and Scenario 5 considers only the CT mechanism, so the individual effects of the two markets can be evaluated separately. Scenario 6 considers the proposed DGCACTM to examine its influence on system operation. Scenario 7 further integrates the MDRM. Finally, Scenario 8 retains the same system configuration as Scenario 7 and introduces a multi-objective scheduling strategy based on a linear weighted sum

of normalized total operating cost and actual carbon emissions, thereby evaluating the trade-off between economic performance and carbon emission reduction.

Table 2. Scenario comparison.

Scenario	1	2	3	4	5	6	7	8
WHR-ORC-P2G		✓	✓	✓	✓	✓	✓	✓
CEHT–grid			✓	✓	✓	✓	✓	✓
GCM				✓				
CTM					✓			
DGCACTM						✓	✓	
MDRM							✓	✓
Multi-objective optimization								✓

Finally, drawing on previous studies of GC–CT and transaction cost modeling [31,33], volume-dependent trading cost functions are developed to characterize the economic incentives associated with different transaction quantities. Net GC purchases are calculated as the prescribed certificate requirement minus the GCs generated from eligible wind power. Following the benchmark-based carbon allowance allocation principle [34,38], the system's carbon quotas are determined by grid electricity purchases, OESI generation, and boiler fuel consumption. Furthermore, considering the mutual recognition between GCs and carbon allowances [38,39], net CT purchases are determined by the difference between actual emissions after carbon capture and the allocated allowances, with an additional GC-related settlement adjustment. Positive trading quantities represent purchases and incur costs, whereas negative values indicate sales and generate revenue. A constant parameter of RMB 100 is adopted in both trading cost functions, which differs from the unit transaction price. The polynomial coefficients remain fixed, while time-dependent saturation thresholds reflect variations across the 24 h scheduling horizon. Finally, the nonlinear trading cost functions are approximated using continuous piecewise linear expressions through SOS2 interpolation.

5.2. Case Study Validation and Analysis of Results

Based on the case study parameters and solution procedure, eight scenarios are constructed, with their results summarized in Figure 6 and Table 3. Scenario 1 serves as the benchmark, with the highest operating cost of 62.566×10^4 RMB and carbon emissions of 85.153 t. Introducing the WHR–ORC–P2G system in Scenario 2 reduces operating cost by 53.76% to 28.931×10^4 RMB and emissions by 11.60% to 75.276 t. The reductions in energy purchase and curtailment costs are 22.544×10^4 and 8.947×10^4 RMB, accounting for 67.03% and 26.60% of the total savings, respectively. This decomposition indicates that the economic improvement mainly arises from reduced energy procurement expenditure and avoided curtailment penalties, consistent with improved waste heat recovery and renewable energy utilization. The magnitude of the savings consequently depends on the adopted energy prices, curtailment penalties, and conversion parameters. Scenario 3 further incorporates CEHT–grid interaction, reducing operating cost by 24.93% to 21.718×10^4 RMB and emissions by 10.91% to 67.063 t relative to Scenario 2. Curtailment cost decreases by 70.82%, whereas energy purchase cost decreases by only 2.63%. These results indicate that CEHT charging and discharging flexibility contributes mainly through improved temporal energy allocation and renewable energy accommodation. Scenarios 4–6 examine GC trading, CT,

and their joint mechanism. Relative to Scenario 3, Scenario 4 reduces operating cost by 2.79% to 21.112 × 10^4 RMB, but emissions increase to 67.698 t. Scenario 5 reduces cost and emissions by 0.58% and 1.47%, respectively, reaching 21.591 × 10^4 RMB and 66.078 t. Scenario 6 achieves the lowest cost among Scenarios 3–6, at 20.920 × 10^4 RMB, while emissions increase to 67.766 t. Thus, trading revenues improve economic performance, but the adopted market incentives do not consistently reduce physical emissions under cost minimization. Introducing the MDRM in Scenario 7 reduces operating cost by 34.25% to 13.755 × 10^4 RMB relative to Scenario 6. Energy purchase and curtailment costs decrease by 4.748 × 10^4 and 1.937 × 10^4 RMB, together accounting for 93.30% of the net savings, while demand response incurs an additional cost of 0.164 × 10^4 RMB. Load shifting and multi-energy substitution allow demand to better match available renewable generation, reducing procurement expenditure and eliminating curtailment under the studied profiles and flexibility limits. Emissions also decrease by 14.83% to 57.715 t. The zero-curtailment outcome is therefore specific to the assumed renewable availability, demand flexibility, and compensation settings. Scenario 8 retains the configuration and constraints of Scenario 7 while assigning equal weights to normalized operating cost and actual emissions. Emissions decrease by a further 53.17% to 27.030 t, while cost increases by 21.06% to 16.652 × 10^4 RMB. Higher energy purchase and equipment operating costs, together with reduced GC revenue, explain the additional expenditure. Since both scenarios maintain zero curtailment, the further emission reduction reflects changes in dispatch decisions. Overall, Scenario 7 achieves the lowest operating cost, whereas Scenario 8 achieves the lowest emissions among the evaluated scenarios, illustrating the economic–environmental trade-off.

Table 3. Results for case study.

Cost (10^4 RMB)	Scenario							
	1	**2**	**3**	**4**	**5**	**6**	**7**	**8**
f_{ab}	15.589	6.642	1.938	1.927	1.937	1.937	0	0
f_{buy}	36.514	13.970	13.602	13.604	13.596	13.608	8.860	10.555
f_{m}	10.462	8.318	6.178	6.200	6.207	6.137	5.578	6.400
f_{GC}	0	0	0	−0.619	0	−0.619	−0.620	−0.216
f_{CT}	0	0	0	0	−0.149	−0.144	−0.231	−0.231
f_{DR}	0	0	0	0	0	0	0.164	0.153
F	62.566	28.931	21.718	21.112	21.591	20.920	13.755	16.652
mCO_2/t	85.153	75.276	67.063	67.698	66.078	67.766	57.715	27.03
ST	5.408	5.572	27.452	31.746	19.842	29.292	71.798	37.986
gap	2.484	2.757	2.573	2.118	2.717	2.829	2.841	2.841

5.3. Benefit Analysis of CEHT–Grid Interaction

To study the specific effects of CEHT–grid interaction on the HACP-IES, a comparative analysis of Scenarios 2 and 3 is conducted in terms of hourly renewable energy curtailment and carbon emissions, as illustrated in Figure 7. As shown in Figure 7a, compared with Scenario 2 without CEHT–grid interaction, Scenario 3 exhibits lower renewable energy curtailment during periods characterized by surplus renewable generation and relatively low load, particularly during nighttime hours. This is because, after CEHT–grid interaction is introduced, CEHTs with relatively light transportation tasks can be scheduled to charge during off-peak periods, thereby absorbing surplus renewable electricity within the HACP-IES and reducing renewable energy curtailment. Meanwhile, Figure 7b shows that the hourly carbon emissions in Scenario 3 are generally lower than those in Scenario 2. Although CEHT charging may increase carbon emissions during certain intermediate-load periods when transportation tasks are relatively intensive, the stored electricity can be discharged

during peak-load periods, thereby reducing grid electricity purchases and suppressing the output of carbon-intensive units. As a result, carbon emissions during peak hours are effectively reduced, thereby reducing the overall carbon emissions of the system.

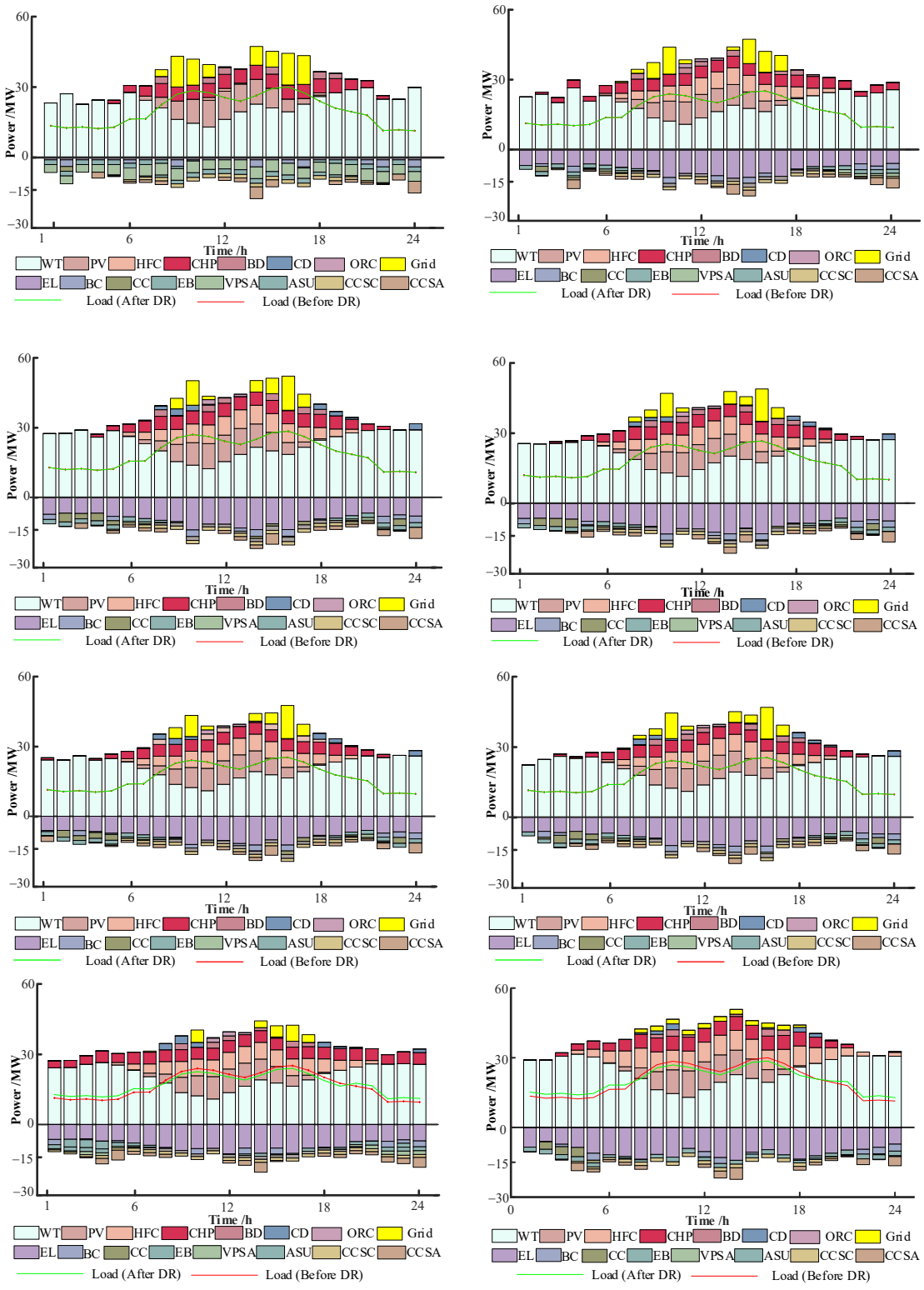

Figure 6. *Cont.*

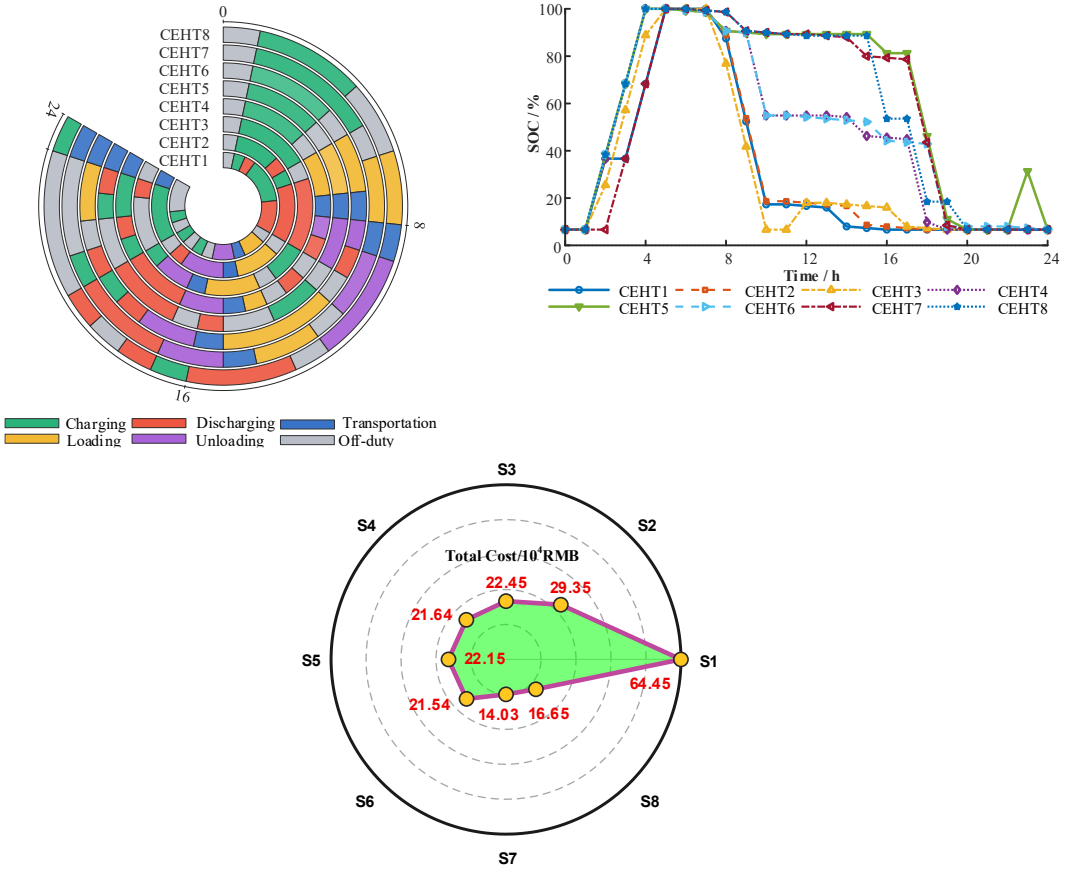

Figure 6. Scheduling results.

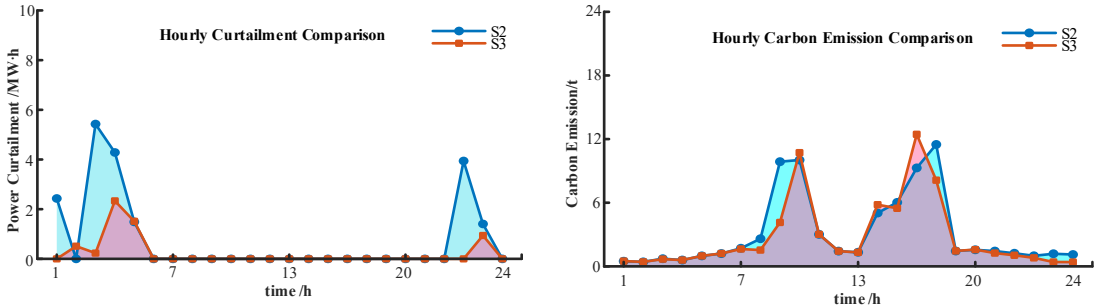

(**a**) (**b**)

Figure 7. CEHT–grid interaction effects: (**a**) renewable energy curtailment; (**b**) hourly carbon emissions.

5.4. Benefit Analysis of Green Certificate and Carbon Trading

The GC and CT costs of the HACP-IES are illustrated in Figure 8. As shown in Figure 8a, the GC cost remains negative throughout the scheduling horizon, indicating that the system generally obtains net revenue from GC trading. During 00:00–05:00, the GC cost fluctuates considerably and reaches its minimum at 06:00. This is mainly attributed to the relatively high WT output and low electrical load during the early hours, which provide conditions for renewable electricity accommodation and GC acquisition. From 06:00 to 11:00, the GC cost gradually increases, reaching its highest level. During this period, the reduction in WT output and the increase in electrical demand weaken the surplus renewable electricity available for GC-related benefits. After 12:00, the GC cost exhibits moderate fluctuations. After 20:00, the GC cost decreases again as WT output recovers, resulting in greater GC revenue. Overall, the GC trading cost is closely related to the balance between renewable generation

and system electricity demand: when renewable electricity is relatively abundant, the GC cost becomes more negative, corresponding to higher GC revenue, whereas insufficient renewable generation leads to a reduction in such revenue. As shown in Figure 8b, the CT cost also remains negative during most periods, indicating that the carbon emission allowances and carbon-offset benefits obtained by the system are generally sufficient to compensate for its carbon emission liabilities. From 00:00 to 09:00, the CT cost remains relatively stable. At 10:00, the CT cost increases noticeably, reflecting an increase in net carbon emission pressure caused by the combined effects of load growth and changes in renewable power output. From 11:00 to 14:00, the CT cost decreases again and remains at a relatively low level. A more pronounced increase occurs during 15:00–17:00, during which the CT cost gradually approaches zero and reaches its maximum at approximately 17:00. This indicates that the carbon-offset contribution of renewable generation and GCs become insufficient to fully compensate for the increase in carbon emissions during this period. After 18:00, the CT cost rapidly decreases, owing to the recovery of renewable generation and the corresponding enhancement in carbon-offset benefits. Overall, the CT cost is jointly determined by renewable power output, electrical and thermal load demands, and the carbon-offset contribution of GCs. When the carbon-offset effect is sufficient to compensate for system emissions, the CT cost remains negative, and the system obtains net carbon trading revenue; conversely, when load-related emissions increase or renewable generation becomes insufficient, the CT cost rises and may approach zero.

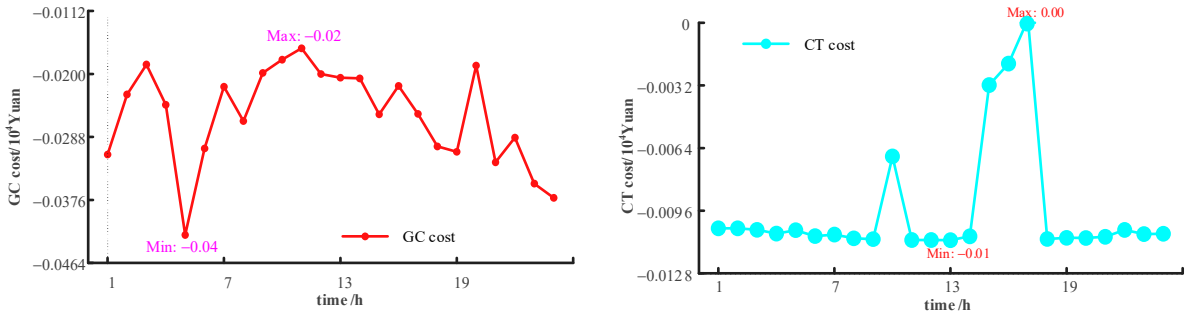

Figure 8. Hourly variations in GC and CT costs: (**a**) green certificate trading cost; (**b**) carbon trading cost.

5.5. Impact Analysis of Wind and Photovoltaic Power Uncertainty

The impacts of wind and photovoltaic power uncertainties are illustrated in Figure 9. As shown in this figure, increasing renewable generation uncertainty can lead to higher output from dispatchable units in the HACP-IES while also indirectly reducing the system's energy curtailment cost and increasing its GC and CT costs. When the uncertainty level remains within a moderate range, flexible resources such as energy storage, power-to-hydrogen facilities, and the CEHTs in the system can effectively mitigate wind and photovoltaic power fluctuations, thereby maintaining a relatively low operating cost. However, as the uncertainty level further increases, the intensified fluctuations in renewable generation result in higher GC and CT costs. Meanwhile, to cope with the potential load losses caused by severe wind and photovoltaic power fluctuations, the HACP-IES must rely increasingly on high-cost regulation measures, such as external electricity and gas purchases or increased output from carbon-intensive units, ultimately leading to a rise in the total operating cost. Therefore, the system cost does not increase monotonically with the level of renewable generation uncertainty. Instead, a relatively low-cost region emerges at moderate uncertainty levels, whereas the operating cost increases markedly near certain uncertainty boundaries.

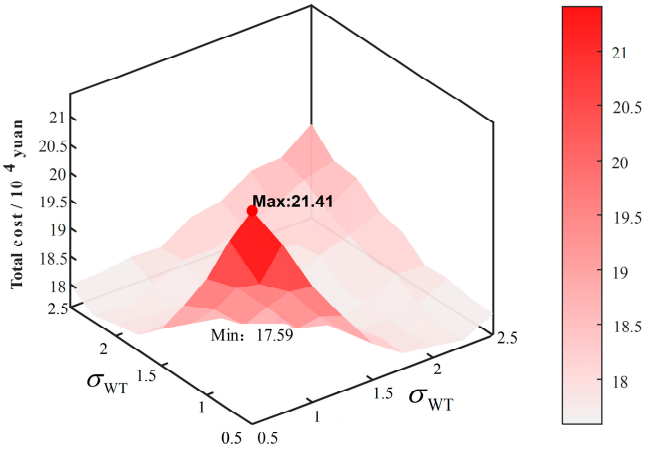

Figure 9. Impact of renewable generation uncertainty on total cost.

5.6. Analysis of Demand Response Results

The MDRM results are illustrated in Figure 10. As shown in Figure 10a, electrical, thermal, and gas loads generally exhibit positive adjustments during 00:00–06:00 and 21:00–24:00, while negative adjustments mainly occur during 07:00–19:00. This pattern indicates that part of the daytime demand is shifted to early-morning and nighttime periods. Shifting electrical demand toward nighttime supports surplus WT output utilization, while reducing daytime demand helps lower electricity procurement expenditure. These adjustments are coordinated with energy storage and CEHT charging and discharging to balance supply and demand across periods. As shown in Figure 10b, thermal load adjustments associated with substitution are predominantly negative, whereas electrical and gas adjustments are generally positive, indicating that part of the heating requirement is reassigned to electricity- and gas-based supply pathways. At the equipment level, the EB converts electricity into heat, while the GB provides gas-to-heat conversion. Their outputs are coordinated with the adjusted electrical, thermal, and gas demands through the system energy balances. This coordination allows suitable energy conversion pathways to be selected according to energy availability, prices, and equipment operating limits. Together, temporal load shifting and cross-energy substitution expand the scheduling flexibility of the HACP-IES. Load shifting improves the timing of energy consumption, while substitution adjusts the energy carriers used to meet demand. Their coordination with energy conversion equipment, storage, and CEHTs supports WT and PV output utilization and contributes to the operating cost and emission reductions observed in the case study.

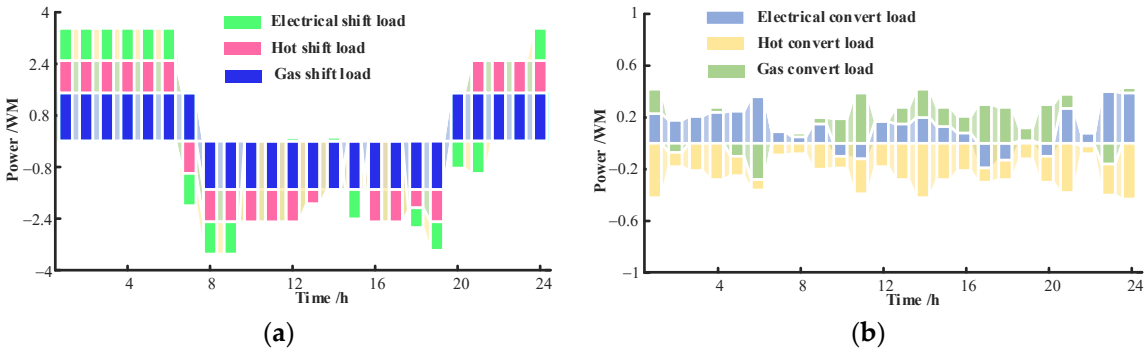

Figure 10. Multi-energy demand response results: (**a**) load shifting; (**b**) cross-energy substitution.

5.7. An Analysis of the Effects of Altitude on the System

Altitude will affect wind and solar power outputs and the output characteristics and energy conversion efficiency of devices in an IES [40–44]. Therefore, the optimization model, after considering the impacts of altitude on system operation costs, is formulated as follows:

$$\begin{cases} F^*(H) = \min\limits_{\boldsymbol{X},\boldsymbol{Y}} \boldsymbol{c}_X^{\mathrm{T}}\boldsymbol{X} + \boldsymbol{c}_Y^{\mathrm{T}}\boldsymbol{Y} + c_0(H) \\ \text{s.t.} \begin{cases} \boldsymbol{A}(H)\boldsymbol{X} + \boldsymbol{B}(H)\boldsymbol{Y} \le \boldsymbol{b}(H) \\ \boldsymbol{C}(H)\boldsymbol{X} + \boldsymbol{D}(H)\boldsymbol{Y} = \boldsymbol{d}(T_a, H) \\ \underline{\boldsymbol{Y}}(H) \le \boldsymbol{Y} \le \overline{\boldsymbol{Y}}(H) \\ \boldsymbol{X} \in \{0,1\}^m,\ \boldsymbol{Y} \in \mathbb{R}^n \end{cases} \end{cases} \tag{28}$$

where $\boldsymbol{X}$ and $\boldsymbol{Y}$ are the discrete and continuous decision variables, respectively; $\boldsymbol{c}_X^{\mathrm{T}}$ and $\boldsymbol{c}_Y^{\mathrm{T}}$ are the coefficient vectors of the discrete and continuous decision variables, respectively; $\boldsymbol{A}$~$\boldsymbol{D}$ are the coefficient matrices of the constraints; $\boldsymbol{b}$ and $\boldsymbol{d}$ are the boundary vectors; $\underline{\boldsymbol{Y}}$ and $\overline{\boldsymbol{Y}}$ are the upper and lower bound vectors, respectively.

Based on Equation (28), an analysis of the dispatch cost is conducted under altitudes ranging from 0 to 3500 m. The specific case study results are shown in Figure 11.

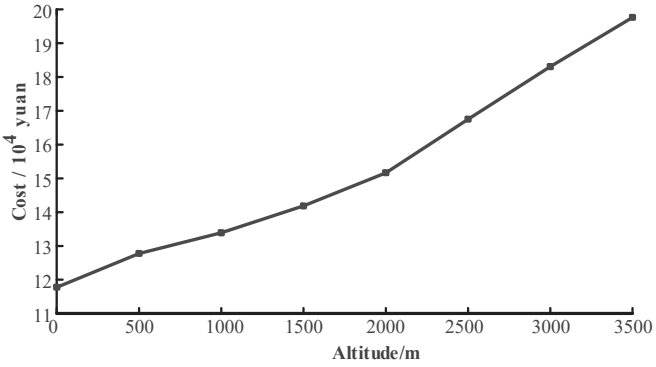

Figure 11. Analysis of effects of altitude on system.

As shown in Figure 11, the total system cost increases with altitude, rising from about 11.8×10^4 yuan at 0 m to 19.8×10^4 yuan at 3500 m. The increase is relatively gradual below 2000 m, where the cost reaches 15.2×10^4 yuan, and becomes more pronounced at higher elevations. These results indicate that higher-altitude operation entails greater operating expenditure, with increased cost sensitivity above 2000 m under the investigated conditions.

5.8. Comparative Analysis of Multi-Objective Optimization Case Studies

To examine the effect of explicitly incorporating carbon emissions into dispatch decisions, Figure 12 compares the hourly operating costs and carbon emissions of S7 and S8 under identical system configurations and constraints. S7 minimizes operating cost, whereas S8 assigns equal weights to daily operating cost and actual carbon emissions, both normalized using the S7 results.

Figure 12a shows that S8 exhibits higher operating costs than S7 at 4 h, 8–10 h, and 24 h but lower costs during 14–17 h. Specifically, compared with S7, S8 has a higher operating cost at 4 h but a lower operating cost at 16 h. Negative hourly costs indicate that revenues exceed expenditures; the less negative values of S8 during 9–10 h therefore represent reduced net revenues.

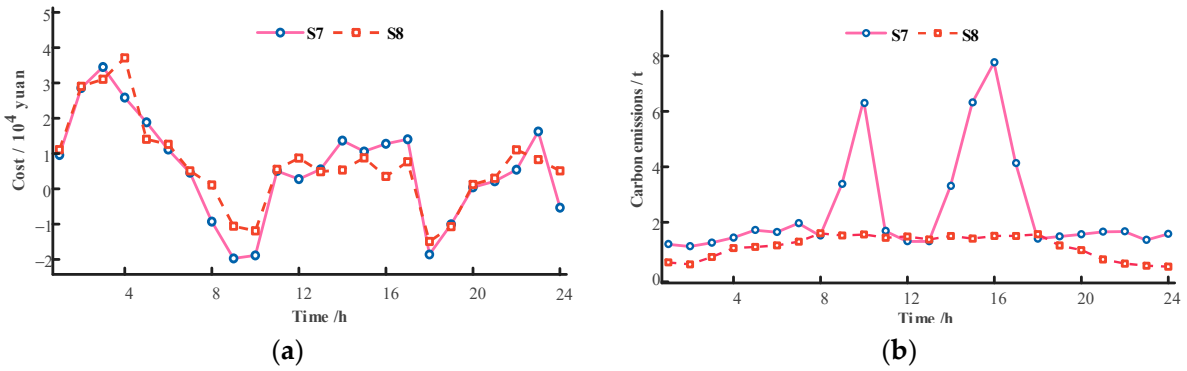

Figure 12. Comparative results of multi-objective optimization case studies: (**a**) hourly operating cost; (**b**) hourly carbon emissions.

Figure 12b shows that S8 substantially suppresses the emission peaks observed in S7 at 10 h and during 15–17 h. At 16 h, emissions decrease from 7.8 t to 1.5 t. Moreover, S8 maintains hourly emissions within 0.4–1.6 t, producing a more stable emission profile. S8 achieves lower emissions during most hours.

Therefore, the multi-objective formulation reduces carbon emissions and suppresses emission peaks while accepting additional expenditure or reduced revenue in selected periods. These results demonstrate that explicitly incorporating actual emissions into the objective strengthens low-carbon scheduling beyond the economic incentives provided by carbon trading alone.

6. Conclusions

To address the challenges of pronounced wind and photovoltaic power fluctuations, low energy utilization efficiency, and the insufficient exploitation of flexible resources in the HACP-IES, this work proposes a low-carbon economic scheduling method incorporating CEHT–grid interaction. The main conclusions are as follows:

1. Through CEHT–grid interaction, the CEHTs in the system can function as mobile energy storage resources while fulfilling their transportation, loading, and unloading tasks. By coordinating their charging, discharging, transportation, and standby states according to variations in renewable generation and load demand, the available scheduling flexibility can be effectively exploited, thereby promoting wind and photovoltaic power accommodation and reducing the carbon emissions of the HACP-IES.
2. The proposed DGCACTM coordinates renewable energy utilization and carbon emission reduction through GC incentives and carbon cost constraints. In the proposed DGCACTM, the interaction between the two markets encourages the preferential use of wind and photovoltaic generation while suppressing the output of carbon-intensive power and heat sources, thereby improving both the economic and low-carbon performance of the HACP-IES.
3. The MDRM enables energy demand to better match the temporal variations in wind and photovoltaic generation, thereby increasing renewable energy utilization and reducing reliance on high-cost and carbon-intensive energy supply. As a result, the total system operating cost and carbon emissions are reduced by 34.25% and 14.83%, respectively, demonstrating the effectiveness of the MDRM.

Author Contributions: Conceptualization, Z.L. and X.Y.; methodology, C.C. and X.Y.; software, C.C.; validation, Z.L. and X.Y.; formal analysis, C.C. and X.Y.; resources, S.H.; data curation, S.H.; writing—original draft preparation, C.C.; writing—review and editing, Z.L. and X.Y.; visualization,

C.C.; supervision, X.Y.; project administration, Z.L.; funding acquisition, Z.L. All authors have read and agreed to the published version of the manuscript.

Funding: This research was funded by the Yunnan Provincial Key Research and Development Program, grant number 202503AA080001, and the Science and Technology Project of China Southern Power Grid Co., Ltd., grant number CGYKJXM20250226. The APC was funded by the authors.

Data Availability Statement: The data used in this study were obtained through an industry-sponsored research project and are not publicly available due to project-related data-use restrictions. The data may be obtained from the corresponding author upon reasonable request, subject to compliance with the relevant project requirements.

Acknowledgments: The authors would like to thank the members of the research group for their valuable guidance, constructive discussions, and support throughout this study.

Conflicts of Interest: The authors declare no conflicts of interest.

Abbreviations

The following abbreviations are used in this manuscript:

HACP-IES	High-Altitude Construction-Park Integrated Energy System
CEHT	Construction Electric Heavy-Duty Trucks
WHR–ORC–P2G	Waste Heat Recovery–Organic Rankine Cycle–Power-to-Gas
DGCACTM	Dynamic Green Certificate and Carbon Trading Mechanism
MDRM	Multi-Energy Demand Response Mechanism
GC	Green Certificate
CT	Carbon Trading

References

1. Liu, Z.; Deng, Z.; He, G.; Wang, H.; Zhang, X.; Lin, J.; Qi, Y.; Liang, X. Challenges and opportunities for carbon neutrality in China. *Nat. Rev. Earth Environ.* **2022**, *3*, 141–155. [CrossRef]
2. Qiu, L.; He, L.; Lu, H.; Liang, D. Systematic potential analysis on renewable energy centralized co-development at high altitude: A case study in Qinghai-Tibet Plateau. *Energy Convers. Manag.* **2022**, *267*, 115879. [CrossRef]
3. Wesonga, R.; Tutesigensi, A.; Moodley, K. Advancing net zero carbon construction: A techno-economic and environmental analysis of onsite microgrids and prosumer energy adoption. *Appl. Energy* **2025**, *398*, 126453. [CrossRef]
4. Mancarella, P. MES (multi-energy systems): An overview of concepts and evaluation models. *Energy* **2014**, *65*, 1–17. [CrossRef]
5. Ayub, M.A.; Hussan, U.; Rasheed, H.; Liu, Y.; Peng, J. Optimal energy management of MG for cost-effective operations and battery scheduling using BWO. *Energy Rep.* **2024**, *12*, 294–304. [CrossRef]
6. Dai, Y.; Zeng, Y. Optimization of CCHP integrated with multiple load, replenished energy, and hybrid storage in different operation modes. *Energy* **2022**, *260*, 125129. [CrossRef]
7. Li, Y.; Wang, J.; Zhou, Y.; Wei, C.; Guan, Z.; Chen, H. Multi-dimension day-ahead scheduling optimization of a community-scale solar-driven CCHP system with demand-side management. *Renew. Sustain. Energy Rev.* **2023**, *185*, 113654. [CrossRef]
8. Dong, H.; Shan, Z.; Zhou, J.; Xu, C.; Chen, W. Refined modeling and co-optimization of electric-hydrogen-thermal-gas integrated energy system with hybrid energy storage. *Appl. Energy* **2023**, *351*, 121834. [CrossRef]
9. Yu, Y.; Han, X.; Yang, M.; Yang, J. Probabilistic prediction of regional wind power based on spatiotemporal quantile regression. *IEEE Trans. Ind. Appl.* **2020**, *56*, 6117–6127. [CrossRef]
10. Turk, A.; Wu, Q.; Zhang, M.; Østergaard, J. Day-ahead stochastic scheduling of integrated multi-energy system for flexibility synergy and uncertainty balancing. *Energy* **2020**, *196*, 117130. [CrossRef]
11. Fu, Y.; Lin, H.; Ma, C.; Sun, B.; Li, H.; Sun, Q.; Wennersten, R. Effects of uncertainties on the capacity and operation of an integrated energy system. *Sustain. Energy Technol. Assess.* **2021**, *48*, 101625. [CrossRef]
12. Li, P.; Wang, Z.; Wang, J.; Yang, W.; Guo, T.; Yin, Y. Two-stage optimal operation of integrated energy system considering multiple uncertainties and integrated demand response. *Energy* **2021**, *225*, 120256. [CrossRef]
13. Lu, J.; Liu, T.; He, C.; Nan, L.; Hu, X. Robust day-ahead coordinated scheduling of multi-energy systems with integrated heat-electricity demand response and high penetration of renewable energy. *Renew. Energy* **2021**, *178*, 466–482. [CrossRef]
14. Li, J.; Xu, L.; Zhang, Y.; Kou, Y.; Liang, W.; Bieerke, A.; Yuan, Z. Economic dispatch of integrated energy systems considering wind–photovoltaic uncertainty and efficient utilization of electrolyzer thermal energy. *Processes* **2024**, *12*, 1627. [CrossRef]

15. Li, S.; Zhang, L.; Nie, L.; Wang, J. Trading strategy and benefit optimization of load aggregators in integrated energy systems considering integrated demand response: A hierarchical Stackelberg game. *Energy* **2022**, *249*, 123678. [CrossRef]
16. Zhu, X.; Yang, J.; Pan, X.; Li, G.; Rao, Y. Regional integrated energy system energy management in an industrial park considering energy stepped utilization. *Energy* **2020**, *201*, 117589. [CrossRef]
17. Miao, B.; Lin, J.; Li, H.; Liu, C.; Li, B.; Zhu, X.; Yang, J. Day-ahead energy trading strategy of regional integrated energy system considering energy cascade utilization. *IEEE Access* **2020**, *8*, 138021–138035. [CrossRef]
18. Pan, C.; Fan, H.; Zhang, R.; Sun, J.; Wang, Y.; Sun, Y. An improved multi-timescale coordinated control strategy for an integrated energy system with a hybrid energy storage system. *Appl. Energy* **2023**, *343*, 121137. [CrossRef]
19. Liu, Z.; Fan, G.; Meng, X.; Hu, Y.; Wu, D.; Jin, G.; Li, G. Multi-time scale operation optimization for a near-zero energy community energy system combined with electricity-heat-hydrogen storage. *Energy* **2024**, *291*, 130397. [CrossRef]
20. Li, Z.; Xia, Y.; Bo, Y.; Wei, W. Optimal planning for electricity-hydrogen integrated energy system considering multiple timescale operations and representative time-period selection. *Appl. Energy* **2024**, *362*, 122965. [CrossRef]
21. Chen, J.; Bie, H.; Wang, J.; Sun, B. Optimization operation method for hydrogen-compressed natural gas-integrated energy systems considering hydrogen-thermal multi-energy inertia. *Results Eng.* **2025**, *25*, 103652. [CrossRef]
22. Borlaug, B.; Muratori, M.; Gilleran, M.; Woody, D.; Muston, W.; Canada, T.; Ingram, A.; Gresham, H.; McQueen, C. Heavy-duty truck electrification and the impacts of depot charging on electricity distribution systems. *Nat. Energy* **2021**, *6*, 673–682. [CrossRef]
23. Speth, D.; Plötz, P. Depot slow charging is sufficient for most electric trucks in Germany. *Transp. Res. Part D Transp. Environ.* **2024**, *128*, 104078. [CrossRef]
24. Çiçek, A. Multi-objective operation strategy for a community with RESs, fuel cell EVs and hydrogen energy system considering demand response. *Sustain. Energy Technol. Assess.* **2023**, *55*, 102957. [CrossRef]
25. Song, S.; Qiu, Y.; Coates, R.L.; Dobbelaere, C.M.; Seles, P. Depot charging schedule optimization for medium- and heavy-duty battery-electric trucks. *World Electr. Veh. J.* **2024**, *15*, 379. [CrossRef]
26. Alam, M.R.; Guo, Z. Co-optimization of charging scheduling and platooning for long-haul electric freight vehicles. *Transp. Res. Part C Emerg. Technol.* **2023**, *147*, 104009. [CrossRef]
27. Bragin, M.A.; Ye, Z.; Yu, N. Toward efficient transportation electrification of heavy-duty trucks: Joint scheduling of truck routing and charging. *Transp. Res. Part C Emerg. Technol.* **2024**, *160*, 104494. [CrossRef]
28. Karmali, L.P.; Gholami, A.; Nezamoddini, N. Integrated optimization of production planning and electric trucks charging and discharging scheduling. *Sustain. Energy Grids Netw.* **2024**, *39*, 101397. [CrossRef]
29. Francis, A.; Fresia, M.; Barabino, E.; Bracco, S. Optimal charging strategy for electric trucks with vehicle-to-grid at a wind-powered electric vehicle charging hub. *Sustain. Energy Grids Netw.* **2025**, *43*, 101899. [CrossRef]
30. Cui, S.; Wu, J.; Gao, Y.; Zhu, R. A high altitude prosumer energy cooperation framework considering composite energy storage sharing and electric–oxygen–hydrogen flexible supply. *Appl. Energy* **2023**, *349*, 121601. [CrossRef]
31. Liu, Y.; Cao, X.; Zhang, Y. Low Carbon Economic Dispatch of a Multi-Principal Integrated Energy System Considering CCS and P2G. *Energy Eng.* **2025**, *122*, 2865–2890. [CrossRef]
32. Ji, X.; Li, M.; Li, M.; Han, H. Low-carbon dispatch of multi-regional integrated energy systems considering integrated demand side response. *Front. Energy Res.* **2024**, *12*, 1361306. [CrossRef]
33. Gao, J.; Shao, Z.; Chen, F.; Lak, M. Multi-energy trading strategies for integrated energy systems based on low-carbon and green certificate. *Electr. Power Syst. Res.* **2025**, *238*, 111120. [CrossRef]
34. Ye, B.; Jiang, J.; Miao, L.; Li, J.; Peng, Y. Innovative Carbon Allowance Allocation Policy for the Shenzhen Emission Trading Scheme in China. *Sustainability* **2016**, *8*, 3. [CrossRef]
35. Qin, C.; Zeng, Y. SR-based chance-constrained economic dispatch for power systems with wind power. *IET Gener. Transm. Distrib.* **2019**, *13*, 2779–2788. [CrossRef]
36. Yang, S.; Zeng, D.; Ding, H.; Yao, J.; Wang, K.; Li, Y. Stochastic security-constrained economic dispatch for random responsive price-elastic load and wind power. *IET Renew. Power Gener.* **2016**, *10*, 936–943. [CrossRef]
37. Wang, J.; Zhong, H.; Xia, Q.; Kang, C.; Du, E. Optimal joint-dispatch of energy and reserve for CCHP-based microgrids. *IET Gener. Transm. Distrib.* **2017**, *11*, 785–794. [CrossRef]
38. Wang, B.; Li, C.; Ban, Y.; Zhao, Z.; Wang, Z. A multi-market equilibrium model considering the carbon-green certificate mutual recognition trading mechanism under the electricity market. *Energy* **2025**, *330*, 136902. [CrossRef]
39. Zhang, J.; Liu, Z. Low carbon economic dispatching model for a virtual power plant connected to carbon capture system considering green certificates-carbon trading mechanism. *Sustain. Energy Technol. Assess.* **2023**, *60*, 103575. [CrossRef]
40. Kang, L.; Lin, S.; Bao, S.; Ma, J. Modeling and analysis of performance degradation in proton exchange membrane fuel cell system for aviation applications. *Aerosp. Sci. Technol.* **2025**, *162*, 110236. [CrossRef]
41. Choi, Y.; Jang, J.J.; Hwang, S.M.; Seo, M.W.; Lee, D.; Jeong, S.K.; Ryu, H.J.; Choi, S.A.; Hwang, B.; Nam, H. Optimizing heat transfer rate for efficient CO_2-to-chemical conversion in CO_2 methanation and CO_2 hydrogenation reactions. *J. CO_2 Util.* **2024**, *81*, 102730. [CrossRef]

42. Zhang, J.; Du, Y.; Yu, J.; Wang, Y.; Wang, C.; Che, D.; Da, Y. The influence of altitude on combustion characteristics within gas-fired boiler by numerical simulation. *Asia-Pac. J. Chem. Eng.* **2023**, *18*, e2880. [CrossRef]
43. Wang, H.X.; Lei, B.; Wu, Y.T.; Zhang, X.M. Operational characteristics and performance optimizations of the organic Rankine cycle under different heat source/condensing environment conditions. *Energy* **2024**, *310*, 133198. [CrossRef]
44. Liu, Z.; Sun, M.; Huang, Y.; Li, K.; Li, Z.; Gan, B.; Xiao, M. Performance of parallel plate-fin heat exchanger for piston aero-engines with front-placed guide plate at high altitude. *Appl. Therm. Eng.* **2022**, *214*, 118829. [CrossRef]

Disclaimer/Publisher's Note: The statements, opinions and data contained in all publications are solely those of the individual author(s) and contributor(s) and not of MDPI and/or the editor(s). MDPI and/or the editor(s) disclaim responsibility for any injury to people or property resulting from any ideas, methods, instructions or products referred to in the content.